

© 2024 IEEE. Personal use of this material is permitted. Permission from IEEE must be obtained for all other uses, in any current or future media, including reprinting/republishing this material for advertising or promotional purposes, creating new collective works, for resale or redistribution to servers or lists, or reuse of any copyrighted component of this work in other works.

Mahmud, Muntasir, Mohamed Younis, Fow-Sen Choa, and Akram Ahmed. "Optical Focusing-Based Adaptive Modulation for Air-to-Underwater Optoacoustic Communication." IEEE, 2024, 1–1.
<https://doi.org/10.1109/JSEN.2023.3340092>.

<https://doi.org/10.1109/JSEN.2023.3340092>

Access to this work was provided by the University of Maryland, Baltimore County (UMBC) ScholarWorks@UMBC digital repository on the Maryland Shared Open Access (MD-SOAR) platform.

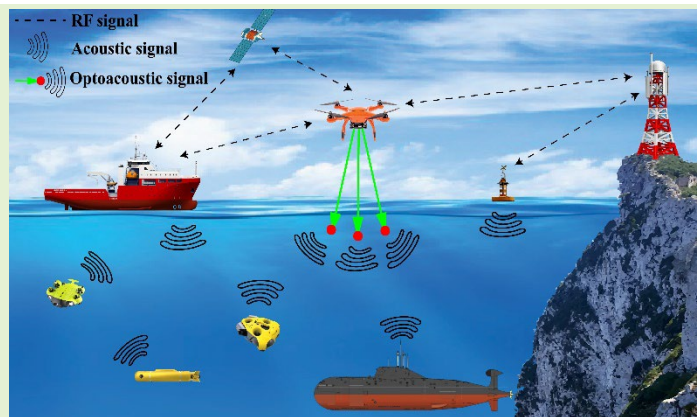
Please provide feedback

Please support the ScholarWorks@UMBC repository by emailing scholarworks-group@umbc.edu and telling us what having access to this work means to you and why it's important to you. Thank you.

Optical Focusing-based Adaptive Modulation for Air-to-Underwater Optoacoustic Communication

Muntasir Mahmud, *Student Member, IEEE*, Mohamed Younis, *Fellow, IEEE*, Fow-Sen Choa, *Senior Member, IEEE* and Akram Ahmed, *Member, IEEE*

Abstract— Nonlinear optoacoustics enable effective communication across the air-water interface. However, the requirement of a high-power laser and the vapor cloud buildup can limit the power efficiency and data rate. Thus, a proper modulation and encoding scheme is necessary. This paper tackles this issue by presenting an Optical Focusing-based Adaptive Modulation (OFAM) technique that can dynamically control the underwater acoustic source (plasma) and acoustic pressure. Specifically, the paper describes two variants of OFAM for a single laser transmitter with stationary focusing (OFAM-1D) and dynamic focusing (OFAM-3D). The data rate of OFAM-1D and OFAM-3D is approximately 6 times and 4.4 times higher than peak detection based on-off keying (PDOOK). Furthermore, both techniques are 137% more power efficient than PDOOK. Studying the bit error rate (BER) in the presence of ambient underwater noises for different node positions has indicated that OFAM can achieve low BER even at a 300 m depth for 50 mJ and 60 mJ laser pulse energy. Moreover, machine learning techniques have been leveraged in the demodulation process for increased robustness. Specifically, the Random Forest model could yield up to 94.75% demodulation accuracy. Our results indicate that OFAM can lead to a new paradigm of air to underwater wireless communication.



Index Terms— Optoacoustic, Photoacoustic, Cross-medium communication, Modulation, Power efficiency, Machine learning.

I. Introduction

WIRELESS communication has advanced so significantly for aerial and terrestrial networks that connectivity is envisioned at a large scale to form an internet of things (IoT). The notion of the Internet of Underwater Things (IoUT) is the undersea extension that is also gaining increased interest [1][2].

Motivation: In the future, the sixth-generation (6G) network is expected to integrate interconnected aerial, terrestrial, and underwater networks that will be fast and more reliable [3]. A critical part of these integrated networks is the communication across the air-water boundary, which links satellites and airborne units, to autonomous underwater vehicles (AUVs), and underwater sensor networks (USNs) [4][5]. Therefore, there is a need for robust high-speed communication links between IoT and IoUT nodes. However, wirelessly connecting aerial and underwater nodes (UWNs) is a serious challenge because no known signal can work well in this cross-medium scenario. The high-frequency radio signals used for IoT communications attenuate very quickly after entering the water. On the other hand, low-frequency radio signals have less attenuation coefficient in water, yet building the needed antennas is very

challenging. Optical signals are known for their ability to propagate over long distances in the air, maintaining high data rates even under varying atmospheric turbulence conditions [6]-[9]. However, when propagating underwater environments, these optical signals encounter significant attenuation, despite their potential for achieving high data rates [10]-[12]. Acoustic signals suffer little attenuation in water and hence are the prime choice for underwater communication. However, acoustic signals do not penetrate the air-water interface well because of the high impedance mismatch. Therefore, the traditional method uses a surface floating node, e.g., a buoy or boat, that is equipped with radio and submerged acoustic transceivers to communicate over the air and in water, respectively. Nevertheless, the mobility of these surface nodes introduces a potential challenge as they may drift away. Moreover, the deployment of these nodes has many significant limitations, encompassing logistical constraints, cost, and security risks.

Cross-medium Communication: Visible light communication (VLC), i.e., free-space optics, is a viable option for forming direct air-water links [13], and can achieve a high data rate within underwater depth of a few meters [14]-[16]. However,

This work is supported by the National Science Foundation, USA, contract #0000010465.

Muntasir Mahmud, Mohamed Younis and Fow-Sen Choa are with the Department of Computer Science and Electrical Engineering, University of Maryland Baltimore County, Baltimore, MD 21250, USA (e-mail:

mmahmud1@umbc.edu; younis@umbc.edu; choa@umbc.edu). Akram Ahmed is with the Computer Engineering Department, King Fahd University of Petroleum and Minerals Dhahran, Saudi Arabia (e-mail: akram@kfupm.edu.sa).

these light beams scatter quickly in water and cannot support long-haul communication. Since the magnetic field is less prone to attenuation across the air-water interface, some studies have explored magnetic induction to form cross-medium links [17][18]. Yet, the communication range using magnetic induction is also limited to 35-70m [19][20]. While microwave-induced thermoacoustic signals can be another alternative [21], the generated signal is not strong enough to support long-haul communication. The optoacoustic process is a more attractive option and enables reaching nodes in deep water from the air, where an acoustic signal is generated when high-intensity light (laser) impinges on a liquid medium like water [22].

The optoacoustic energy transfer mechanism can be classified into linear and nonlinear, depending on the energy density and irradiance imparted to the water medium. In the nonlinear optoacoustic process, the energy conversion rate is higher than the linear counterpart, and hence, the generated acoustic signal is stronger and can propagate long distances. The acoustic source level (SL) is required to be greater than 180 dB for many naval applications. SL over 210 dB is reported using the nonlinear optoacoustic process in [23], making it an attractive option. Nonetheless, using optoacoustic signals for communication is challenging because it involves two distinct signal types, optical in air and acoustic in water. A high-power laser is required for the optical breakdown, which results in the formation of vapor clouds in the vicinity of the laser focus point [24]. With the increase of the laser repetition rate, such a vapor cloud can become intense enough to preclude acoustic signal generation. Therefore, non-traditional modulation techniques are needed for effective optoacoustic links.

Optoacoustic Modulation: On-off keying (OOK) is the most popular modulation technique in the realm of optical communications and is known for its bandwidth efficiency and high bit-rate. In OOK, a "0" bit is represented by zero intensity, and a "1" bit is represented by positive intensity. However, due to the vapor cloud formation in nonlinear optoacoustic communication OOK cannot achieve a high data rate during consecutive transmission of "1" bits in a short period of time [25]. On the other hand, pulse position modulation (PPM), which is more energy efficient than OOK [26], may transfer data using a high repetition rate laser without producing a vapor cloud. Yet, PPM is not bandwidth efficient because each M bits are sent over $L = 2^M$ time slots. Thus, the data rate diminishes as M grows despite using a high repetition laser. Moreover, both OOK and PPM require precise time synchronization between the transmitter and receiver, which is extremely difficult to achieve in underwater environments. Although the differential pulse position modulation (DPPM), its improved version, IDPPM, and the differential amplitude pulse position modulation (DAPPM) techniques are more bandwidth efficient than PPM, there is a potential for vapor cloud buildup which limits their achievable data rate. Our OFAM technique overcomes the limitation of existing modulation schemes [27]. The main idea of OFAM is to create different plasma shapes by dynamically adjusting the laser focal spot in the water to generate various acoustic signal strengths. This paper further exploits dynamic laser modulation with pulse energy-focusing combinations to increase the data rate.

Contribution: This paper tackles the aforementioned challenges of optoacoustic modulation. Two methods are proposed for a single laser transmitter with stationary focusing (OFAM-1D) and dynamic focusing (OFAM-3D) to overcome the data rate

limitation due to the vapor cloud effect and also achieve higher power efficiency than PDOOK. In OFAM-1D, a minimum delay between two consecutive laser pulses is introduced to enable communication with a higher repetition rate laser. The simplicity of OFAM-1D makes it suited for applications that do not need high data-rates. On the other hand, OFAM-3D is designed to avoid vapor cloud formation by transmitting each laser pulse to a different focal point. OFAM-3D trades off complexity for achieving the high data rate and power efficiency. We have conducted prototype-based experiments to assess the effectiveness of OFAM-1D and OFAM-3D in mitigating the effect of vapor clouds. To validate the data rate improvement, we have done a text communication simulation with ASCII characters. The results show OFAM-1D and OFAM-3D, respectively, have about 6 and 4.4 times higher symbol rate than PDOOK using 320 Hz laser repetition rate and both are 137% more power efficient than the PDOOK.

OFAM is in essence a multilevel amplitude based scheme where the number of levels (modulation order) depends on the number of different bits that can be transmitted. Our proposed methods generate these distinct bits based on different laser modulation parameters. The simplest forms of OFAM having two amplitude levels can transmit three bits ("1" bit and "2" bit and additional "0" bit, meaning no intensity) and relies on acoustic signal strengths for demodulation. However, it can be challenging to demodulate the acoustic signals generated by higher-order OFAM with three or more levels in complex underwater environments. Therefore, we have studied the effect of underwater communication range on BER. The simulation results have demonstrated the robustness of the third order OFAM against the underwater ambient noise. We have tackled the higher-order OFAM demodulation challenge using machine learning (ML) models by considering both time and frequency domain features. To validate the ML-based demodulation technique, we have considered the ninth order OFAM, i.e., with eight different acoustic signal levels, and four cases of UWN positioning relative to the laser beam. The Random Forest model could achieve up to 94.75% demodulation accuracy and requires 0.58 ms per signal after feature extraction. Therefore, ML-based demodulation can enable the use of a higher order OFAM and consequently increase the data rate. In summary, the main contributions of this paper are:

- Develop an effective optoacoustic modulation scheme to mitigate the effect of vapor cloud and enable uninterrupted acoustic signal generation using the least delay between consecutive laser pulses or the minimum distance between consecutive focal points.
- Propose a novel ML-based optoacoustic demodulation scheme using time and frequency domain features.
- Conduct extensive experimental study on controlling the peak-peak acoustic signal generation by varying the focal spot and laser pulse energy.
- Analyze the bit-rate, symbol rate, power efficiency and BER of nonlinear optoacoustic links under varying underwater node positions.

The paper is organized as follows. Section II covers the related work. The optoacoustic signal generation, control and communication challenges are discussed in Section III. The applicability of traditional modulation and encoding techniques to optoacoustic communication is analyzed in Section IV. Section V describes OFAM in detail. Section VI reports the experimental results. The paper is concluded in Section VII.

II. RELATED WORK

Communication across the air-water interface has drawn growing interest in recent years [4][28]. Links from underwater to the air have been established using translational acoustic-radio frequency communication technology [29][30] and visible light [31][32]. However, little progress has been made to support communication from the air to the underwater, especially when recipients are deep in the water. This paper contributes in filling the technical gap using optoacoustic signals. The optoacoustic effect is more popular in the areas of the medical field [33]-[36] and also used for underwater material classification [37], mine detection [38], remote sensing [39] and UWN localization [40]. Although many studies have been conducted to characterize and control the generated acoustic signals [23][24][35][36][41]-[53], the use of optoacoustic effect to support cross-medium communication is relatively new [22][27][54]-[56].

In recent years, there has been some notable work on air-water optoacoustic communication. For long-haul links, the nonlinear optoacoustic signal generation is more effective than the linear process, where a greater source level is achieved. Blackmon and Antonelli demonstrated a means of deterministically controlling the spectrum of the underwater acoustic signal by varying the laser pulse repetition rate [24]. They suggested to use a M-ary frequency shift keying and frequency-hopping direct sequence spread spectrum technique by controlling the laser repetition rate. A similar idea is pursued, in [54], to demonstrate voice transmission over an optoacoustic link. However, varying the laser repetition rate method is not bit rate and power efficient as it requires several laser pulses to transmit a single symbol and the overall acoustic spectrum remains broadband. Moreover, a high repetition rate cannot be used due to vapor cloud formation. Ji et al. [55] have proposed a method to minimize the laser energy requirement for optoacoustic communication using floating low-cost passive relays, which absorb laser pulse energy to generate the acoustic signal by thermal expansion-contraction. However, deploying these relays is logistically complicated and the thermal absorption is in essence a linear optoacoustic process and supports only short ranges.

The U.S. Naval Research Laboratory (NRL) measured the acoustic pulse propagation up to 300 m distances for acoustic SL of about 190 dB [49]. They demonstrated acoustic pulse duration control by plasma shape control. As a result, NRL's variable pulse duration method improves the spectral separation and is more robust against noise and propagation delay errors. Recently we have proposed a peak detection based OOK modulation (PDOOK) technique to overcome the complexity of the hybrid natures of optoacoustic signals, i.e., modulating a laser beam and demodulating the corresponding acoustic signal [56]. However, existing nonlinear optoacoustic modulation techniques are vulnerable to vapor cloud formation. Therefore, communication from air using the nonlinear optoacoustic effect requires proper modulation and encoding techniques to mitigate the impact of vapor clouds and increase power efficiency.

III. OPTOACOUSTIC SIGNAL GENERATION AND CONTROL

A. Laser-induced Optical Breakdown

The optoacoustic method can generate underwater acoustic signals from a remote, aerial location using a high-intensity laser source. In the nonlinear optoacoustic process, laser-

induced optical breakdown leads to plasma formation at locations where the breakdown threshold is exceeded. This plasma formation is associated with a breakdown shockwave and the subsequent cavitation bubble expansion-collapse shockwaves, which generate the acoustic signal. The breakdown threshold, plasma formation, and acoustic signal generation depend on the laser parameters, as discussed in detail in [22]. In order to generate acoustic signals in the water, the irradiance threshold values are in the order of 10^{11} W/cm² for a few nanosecond pulse durations and rise up to 10^{13} W/cm² for a 100 femtosecond pulse duration laser source [35]. Laser irradiance (I) can be measured from the laser pulse energy (E), pulse duration (τ_L) and the focal spot area (A_f),

$$I = \frac{E/\tau_L}{A_f} \quad (1)$$

The focal spot area, $A_f = \pi\omega_0^2$, with spot radius,

$$\omega_0 = \frac{\lambda f M_l^2}{\pi (D/2)} \quad (2)$$

where, λ is the wavelength of the laser beam, f is the focal length of the lens, D is the diameter of the laser beam and M_l^2 is the beam propagation ratio. Having M_l^2 equals to 1 implies the focused spot is diffraction limited under the perfect Gaussian condition. Thus, the diffraction-limited focus spot radius is,

$$\omega_0 = \frac{2\lambda}{\pi} \cdot \frac{f}{D} \quad (3)$$

The ratio of focal length to beam diameter, i.e., $\frac{f}{D}$, is known as the f -number ($f/\# = \frac{f}{D}$). We will use $f/\#$ to refer to the f -number of a specific beam. Based on (1) and (3), we can get the laser irradiance using,

$$I = \frac{\pi E}{4\lambda^2 \tau_L (f/D)^2} \quad (4)$$

It is observed from (4) that increasing the laser pulse energy or decreasing the f -number will increase the laser irradiance in the focused spot to generate plasma.

B. Plasma Shape and Size Control

The shape and size of the laser-induced plasma are significant because the strength and directionality of the generated acoustic signal depend on them. The length of the generated plasma (z_{max}) reached at maximum irradiance for laser pulse with Gaussian shape is [41],

$$z_{max} = \frac{\pi\omega_0^2}{\lambda} \sqrt{\beta - 1} \quad (5)$$

where $\beta = \frac{E}{E_{th}} = \frac{I}{I_{th}}$ is the normalized laser pulse energy, and $\frac{\pi\omega_0^2}{\lambda}$ is the Rayleigh range. Substituting the values of ω_0 from (3) into (5) we get,

$$z_{max} = \frac{4\lambda(f/D)^2}{\pi} \sqrt{\beta - 1} \quad (6)$$

The dependency of maximum plasma length (z_{max}) on the focusing angle (θ) is given in [36] as,

$$z_{max} = \frac{\lambda}{\pi \tan^2 \frac{\theta}{2}} \sqrt{\beta - 1} \quad (7)$$

The dependence of plasma length on the laser wavelength, pulse energy, focusing angle and f -number is evident in (5)-(7); however, the dependence of z_{max} on the laser pulse duration is implicit. Since the breakdown threshold varies with pulse

duration, determining β requires knowledge of the breakdown threshold E_{th} or I_{th} at the pulse duration of interest, which affects z_{max} . This plasma length is dependent on the laser focusing geometry. For example, decreasing the f -number will reduce the focus spot radius; thus, the plasma length will decrease for a fixed laser pulse energy. Hence, the laser focusing geometry is critical because a higher focusing angle (lower f -number) can generate more spherical single-core plasma. On the other hand, loose focusing (high f -number) can generate a cylindrical-shaped plasma or multiple weak plasmas. Based on (5)–(7), the plasma will be more elongated for higher energy laser pulses. Sinibaldi et al. [53] have analyzed the plasma sphericity index (ζ) as a function of laser pulse energy (E) and focusing angle (θ), where $\zeta(E, \theta) = w/z_{max}$. The results show that the sphericity index is around 0.7–0.8 at the threshold energy and the plasma is more spherical for higher focusing angles. However, the sphericity index is capped to 0.4 at large energies, regardless of the focusing angle. The laser irradiance and focal spot radius are significant for generating different plasma shapes and sizes because changing the laser pulse energy or focusing geometry means varying the laser irradiance in the focal spot.

C. Acoustic Signal Control

The laser-induced breakdown and bubble collapse cause shockwaves during the nonlinear optoacoustic process. During plasma formation, first, the breakdown shockwave emission occurs. Then, the generated cavitation bubbles expand, collapse and re-expand, which leads to the creation of additional acoustic signals of frequencies that depend on the bubbles' size. The number of acoustic transients generated by the cavitation bubble depends on the total mechanical energy made available by the laser pulse energy. The strength and directionality of the generated acoustic signal depend on the plasma's shape and size. A shorter plasma length implies a more spherical shape and as the plasma length elongates, it becomes more cylindrical in shape. A spherical acoustic source can generate isotropic pressure in all directions, but the pressure becomes more anisotropic with the elongation of the plasma. A narrowband laser source with lower pulse energy generates almost the same acoustic pressure in all directions, but as the pulse energy increases, the pressure increases from 0° to 90° [49]. The pressure difference in all directions can be decreased by making the plasma shape more spherical. Moreover, the acoustic signal's frequency spectrum, acoustic pulse duration and radiation pattern can be varied by pulse energy [49].

The generated acoustic signal also depends on the laser beam focus. Because smaller focal lengths can produce short and highly absorbing plasmas, a well-localized energy deposition at a low breakdown threshold is possible. In addition, large focusing angles (smaller focal lengths) are associated with a high conversion efficiency into mechanical energy and, thus, have a greater potential to induce higher acoustic pressure. Therefore, decreasing the focal spot radius or f -number can generate more compact plasma with a stronger emission for a fixed laser pulse energy. By increasing the laser focusing angle, Tian et al. [52] demonstrated that the discrete and irregular plasma created in numerous locations could be transformed into continuous and stable plasma with a single core fixed at the laser focal point. Thus, the generated acoustic signal strength and directionality can be adjusted by controlling the plasma shape and size, which in turn can be controlled by varying focusing or laser pulse energy.

D. Communication Challenges

Nonlinear optoacoustic signal generation is more effective for long underwater reach than the linear one because the generated acoustic source level is higher. However, the characteristics of the produced underwater acoustic signals are challenging to control, making it hard to design modulation schemes. One of the difficulties in nonlinear optoacoustic communication is the requirement of the laser energy to be concentrated in a small underwater spot for optical breakdown. Another challenge is the resulting acoustic signal's broadband spectrum because it restricts the communication range and makes frequency-based modulation quite challenging. Overall, the generated acoustic signal has a spectrum up to a few MHz [47]. However, the shape and volume of the plasma affect the energy spectral density of the acoustic signal, with more elongated plasma volumes producing longer-duration acoustic pulses with higher energy at low frequencies. The trade-off for generating elongated plasma using a single laser transmitter is that it requires higher energy with a proper focusing angle [49]. Moreover, a higher pulse energy laser can generate larger acoustic SL which in turn enables a greater communication range. Thus, a suitable modulation and encoding technique is needed that also optimizes the power consumption.

A significant obstacle to the achievable bit-rate of nonlinear optoacoustic communication is the formation of vapor clouds in the vicinity of the laser focal point in water. This vapor cloud blocks the acoustic signal generation during higher repetition laser transmission in some laser pulse intervals [24]. Thus, a certain delay is needed between two successive laser pulses to avoid the effect of vapor cloud. In addition to the concern about vapor cloud effect, the interaction between successive laser pulses is possible when the pulse repetition rate is higher than 1000 Hz [46].

IV. ANALYSIS OF TRADITIONAL MODULATION AND ENCODING TECHNIQUES FOR OPTOACOUSTIC COMMUNICATION

In contrast to radio, acoustic, and visible light, optoacoustic communication involves two different signal types, optical (laser beam) and acoustic. Hence, traditional modulation and encoding techniques cannot be fine-tuned to boost the bit rate for optoacoustic communication. Moreover, a lower repetition rate laser must be used to preclude vapor cloud buildup. The maximum repetition rate (R_{max}) is the highest repetition rate at which the acoustic signals are generated for all corresponding laser pulses. R_{max} can be determined by transmitting continuous "1" bits (laser pulse) and increasing the laser repetition rate until we observe that an acoustic signal is missing at the time a laser pulse was transmitted. In addition, a higher laser pulse energy is required to achieve a longer communication range. Thus, the number of "on" chips ("1" bit) should be minimized during data transmission in order to reduce power consumption. In this section, we analyze how traditional optical modulation and encoding techniques perform when utilizing optoacoustic transmissions. Particularly, we consider OOK, which is used in [56], and other conventional techniques such as PPM, DPPM, IDPPM, and DAPPM. We also highlight key limitations that we overcome in our OFAM approach in Section V.

A. Bit-rate Analysis

OOK is the most popular modulation technique in optical communications. However, it has the potential for several consecutive "1" bit transmissions, as shown in Table I. Thus, the bit rate using the OOK technique will be capped by R_{max} . Although the PPM technique is known for its power efficiency, it is not bandwidth efficient where each group of M bits is sent over $L = 2^M$ time slots. However, PPM can transmit data with a comparatively higher repetition rate than OOK because, in PPM only a single "1" bit and $L - 1$ "0" bits are transmitted. Thus, there is a delay between two "1" bits of two PPM symbols during transmission. However, there is a possibility of two successive "1" bits scenarios, e.g., if two consecutive symbols are "00000001" and "10000000" for $M = 3$. Let $R_{max,PPM}$ be the highest repetition rate at which two consecutive "1" bits can be transmitted in PPM without facing the vapor cloud effect. $R_{max,PPM}$ increases with M and is higher than R_{max} . For example, $R_{max,PPM}$ is higher for $M = 7$ than for $M = 3$ because there is more delay ("0" bits) between two laser pulses ("1" bits). However, the average bit length per symbol also increases with M , which limits the bit-rate. $R_{max,PPM}$ is also constrained by vapor cloud formation. Basically, the time interval between two consecutive "1" bits decreases as the laser repetition rate increases, which boosts the potential of vapor cloud buildup and interference among successive laser pulses.

In DPPM, all the "0" bits are deleted following the "1" bit from the corresponding PPM symbol. DPPM is more power efficient than OOK and more bandwidth efficient than PPM. Since DPPM has the potential for several consecutive "1" bits transmissions in nonlinear optoacoustic communication, the maximum repetition rate using the DPPM technique will also be limited. Therefore, the maximum repetition rate of the DPPM is the same as OOK. Meanwhile, IDPPM is derived from DPPM by adding one zero before each DPPM symbol [57]. Hence the worst-case scenario for the IDPPM technique is repetitive "01" bits transmission, e.g., the "010101..." bit sequence, and consequently, the maximum repetition rate for IDPPM is twice of R_{max} because there is at least one "0" bit between two "1" bits.

DAPPM is a combination of pulse amplitude modulation and DPPM. Therefore, the data is transmitted by varying the symbol length and the pulse amplitude. DAPPM provides better bandwidth efficiency and higher transmission capacity than the other modulation PPM variants [58]. Similar to DPPM and IDPPM, a DAPPM symbol has only one "on" chip at the end of the symbol. The amplitude of such a chip is selected from the set $\{1, \dots, \alpha\}$. The length of a DAPPM symbol varies from $\{1, \dots, L\}$ and a block of $M = \log_2(\alpha \times L)$ source bits are mapped to one of 2^M distinct symbols. The laser repetition rate is also limited to R_{max} because of the potential for several consecutive "on" bits transmissions.

The properties of OOK, PPM, DPPM, IDPPM and DAPPM are summarized in Table I. The average bit length per symbol for the DAPPM technique is 2.5, which is lower than OOK. Thus, the data rate of DAPPM should be higher than other techniques for the same laser repetition rate. However, dynamically varying the laser pulse energy for the DAPPM technique in nonlinear optoacoustic communication is challenging and usually requires multiple laser sources depending on the value of α . The bit-rate of OOK, PPM, DPPM, IDPPM, and DAPPM is calculated by,

TABLE I Mapping of source bits for $M = 3$ into different modulation techniques symbols for optoacoustic communication.

Source Bits $M = 3$	OOK $M = 3$	PPM $L = 8$	DPPM $L = 8$	IDPPM $L = 9$	DAPPM $L = 4, \alpha = 2$
000	000	10000000	1	01	1
001	001	01000000	01	001	01
010	010	00100000	001	0001	001
011	011	00010000	0001	00001	0001
100	100	00001000	00001	000001	2
101	101	00000100	000001	0000001	02
110	110	00000010	0000001	00000001	002
111	111	00000001	00000001	000000001	0002

$$B_{OOK} = R_L \quad (8)$$

$$B_{PPM} = \frac{M \times R_L}{2^M} \quad (9)$$

$$B_{DPPM} = \frac{2 \times M \times R_L}{2^M + 1} \quad (10)$$

$$B_{IDPPM} = \frac{2 \times M \times R_L}{2^M + 3} \quad (11)$$

$$B_{DAPPM} = \frac{2 \times \alpha \times M \times R_L}{2^M + \alpha} \quad (12)$$

where, R_L denotes the laser repetition rate. The maximum value of R_L without causing the vapor cloud effect for OOK, DPPM and DAPPM is R_{max} , for IDPPM is $2 \times R_{max}$ and for PPM is $R_{max,PPM}$. The value of R_{max} should be fixed, yet $R_{max,PPM}$ is variable and should increase with M . The bit-rate of all these techniques except OOK decreases as M increases, which is observed from (9)-(12). Moreover, none of these techniques can achieve a high bit-rate due to their limited laser repetition rate for nonlinear optoacoustic communication.

B. Power Efficiency Analysis

All the techniques except OOK have only one "on" chip ("1" bit) per symbol, as shown in Table I. If the probability of "0" and "1" bits occurrence in the data is the same, the power efficiency of the DPPM with respect to OOK will be [59],

$$P_{DPPM/OOK} = \left(1 + \frac{M-2}{M}\right) \times 100\% \quad (13)$$

Equation (13) indicates that DPPM becomes more power efficient than OOK as M increases. The power efficiency of the PPM and IDPPM relative to OOK is the same as (13) because they also have only one "on" chip in each symbol. Therefore, PPM, DPPM and IDPPM have the same power efficiency. In the case of DAPPM, there is only one "on" chip per symbol, but the amplitude of the "on" chip varies. The amplitude value usually increases linearly. For example, if the first amplitude is $a_1 = P_C$, the other amplitudes should be $a_2 = 2P_C$, $a_3 = 3P_C, \dots, a_\alpha = \alpha \times P_C$. If the amplitude in the OOK technique is the same as a_1 , the power efficiency of the DAPPM relative to OOK can be calculated as,

$$P_{DAPPM/OOK} = \left(1 + \frac{M-\alpha-1}{M}\right) \times 100\% \quad (14)$$

Equation (14) indicates that DAPPM becomes more power efficient than OOK as M increases and α decreases. Compared to PPM, DPPM and IDPPM, the DAPPM technique is less power efficient for the same M value. While all techniques

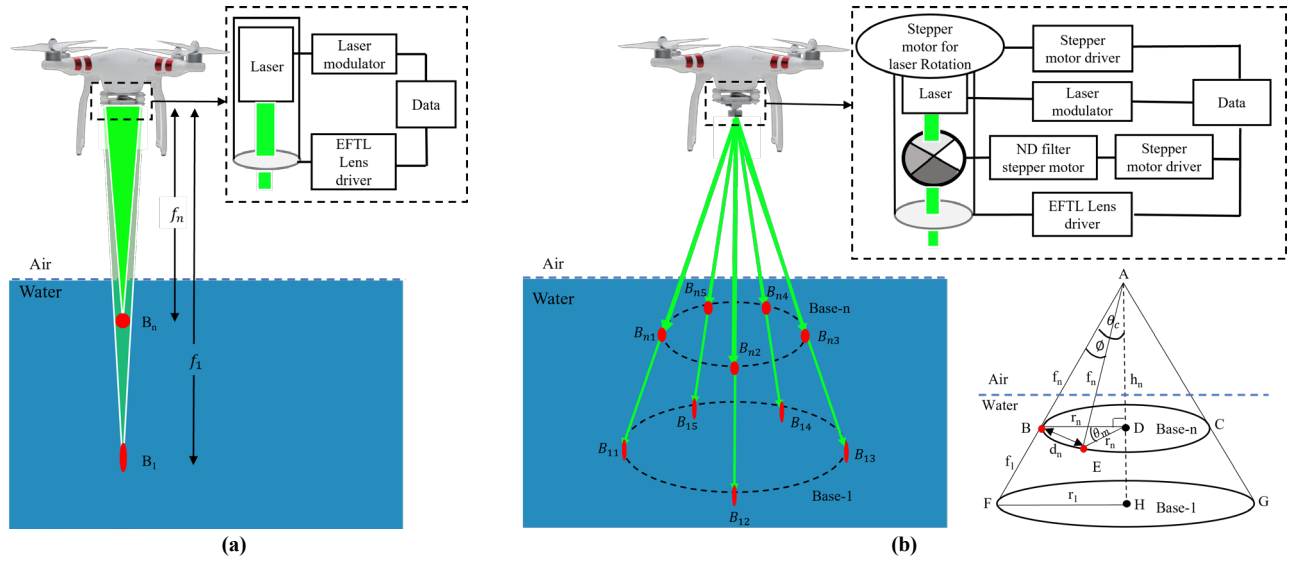


Fig. 1. The focal length of OFAM techniques varies from 1 to n using EFTL lens depending on the data. (a) OFAM-1D is illustrated using two focal lengths. The vapor cloud effect is mitigated by introducing a delay, T_v , between two consecutive laser beams. (b) with two focal lengths, OFAM-3D transmits each laser beam to different locations on two circular bases. Stepper motors are used for dynamic focusing to different locations and rotate a neutral density filter to vary the laser pulse energy. A minimum distance (d_v) is kept between two adjacent focal points to preclude the vapor cloud effect when the T_v delay is not applied.

become more power efficient for higher values of M , i.e., $M > 2$, the bit-rate decreases.

V. OPTICAL FOCUSING-BASED ADAPTIVE MODULATION

Our OFAM modulation technique, which has been introduced in [27], leverages advanced electrically focus-tunable lenses. The main idea of OFAM is to create different plasma shapes by varying the laser irradiance in the focal spot to generate various acoustic signal levels. We are considering the laser-induced plasma as the antenna for the underwater acoustic source, where the antenna shape can be changed by varying the laser pulse energy and/or focusing point. In this section, we extend the basic concept and present two variants of the OFAM technique based on the location of the focal point. In addition, machine learning based demodulation is introduced for higher order OFAM to improve demodulation accuracy.

A. Fixed Focusing Position (OFAM-1D)

The generated acoustic signal depends on the shape of the acoustic source (plasma), as discussed in Section III. Therefore, different acoustic signal strengths can be generated by varying the laser focusing length (f) in water. OFAM-1D considers a single stationary laser transmitter with a fixed vertically downward focusing position and dynamically controls the focal length using electrically focus-tunable lenses (EFTL), as shown in Fig. 1(a). These advanced lenses are driven by electrical current, and the focal length is a function of the electrical current [60]. The stronger the current is, the shorter the focal length becomes. Thus, the focal length can be changed dynamically to modulate the laser beam to generate different acoustic pressure underwater. For n lens settings, we will use the configuration number to reflect the shortest achievable focal length. For example, for $n = 4$, f_1 is the longest and f_4 is the shortest focal length. Fig. 1(a) illustrates two different focus lengths ($n = 2$) at positions B_1 and B_n . At position B_n , the laser beam is more tightly focused using f_n focal length, which is shorter than the f_1 focal length. Thus, the focus spot radius is

smaller and the laser irradiance is higher at position B_n than at position B_1 , and consequently, the generated acoustic pressure should be higher for f_n than f_1 . Generally, a UWN can receive multiple signal strengths depending on the number of focus length settings (n).

The number of "on" chips should be minimized in nonlinear optoacoustic communication to reduce the probability of vapor cloud formation and increase power efficiency. Therefore, the OFAM-1D symbols have only one "on" chip at the end of the symbol, whose amplitude is selected from the set $\{1, \dots, n\}$. The OFAM-1D symbols are derived from DAPPM where $\alpha = n$ and by adding extra "0" bits before the DAPPM symbols. The "0" bits are added to include a sufficient delay between two laser pulses ("on" chips) and avoid vapor cloud formation. This will enable data transmission with a higher repetition rate where the chip duration (T_c) is lower. The required number of "0" bits (N_0) for vapor cloud delay (VCD) is:

$$N_0 = \begin{cases} \left\lceil \frac{R_L}{R_{max}} - 1 \right\rceil, & \text{If } R_L > R_{max} \\ 0, & \text{Otherwise} \end{cases}$$

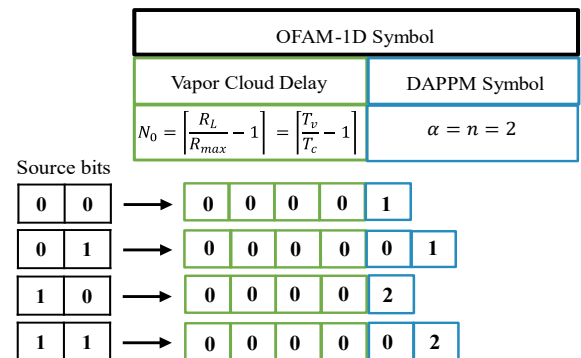


Fig. 2. Illustrating the OFAM-1D symbol structure with an example for $M = 2$, $n = 2$ and $N_0 = 4$.

N_0 can also be represented by $\left\lceil \frac{T_v}{T_c} - 1 \right\rceil$, where the time required for VCD (T_v) and T_v is equal to $\frac{1}{R_{max}}$. Hence, the data rate of OFAM-1D grows when R_L increases and T_v decreases.

On the transmitter side, shown in Fig. 1(a), the OFAM-1D symbol bits corresponding to the data depends on the laser modulator and EFTL lens driver. This laser modulator and EFTL lens driver are connected to the laser and EFTL lens, respectively. There should be $n + 1$ different bits present in the data and based on the data bits a modulated laser beam is transmitted underwater. For example, if $n = 2$, three different bits ("0" bit, "1" bit and "2" bit) appear in the encoded data. In such a case, data = "0" bit means no laser pulse, data = "1" bit means laser pulse will be focused with f_1 focal length and data = "2" bit means laser pulse will be focused with f_2 focal length. Therefore, the EFTL driver will flow a weaker electrical current to the EFTL lens to create a longer focal length (f_1) for a "1" bit and flow a stronger electrical current to create a shorter focal length (f_2) for a "2" bit. However, the electrical current flow to the EFTL lens will not be changed for a "0" bit where no laser pulse will be transmitted. Thus, different acoustic pressure will be generated underwater based on the data.

On the receiver side, the UWN will receive only one acoustic signal for each symbol and demodulate the received signal compared with threshold values and the delay since receiving the previous signal. In order to calculate the threshold values, some control bits (C_b) will be transmitted at the beginning of the data transmission. C_b should be a mix of all the different bits which is already known by the UWN. For example, $C_b = [1002]$ or $C_b = [1001002002]$ could be used for $N_0 = 2$ and $n = 2$. Thus, the UWN can calculate the first threshold (T_{h1}) by dividing the average peak-peak pressure generated from all the "1" bits in C_b by 2. Similarly, the second threshold (T_{h2}) can be calculated by adding the peak-peak pressure generated by all the "1" and "2" bits and dividing by the total number of "1" and "2" bits present in C_b .

OFAM-1D symbols have unequal durations and do not require symbol synchronization, similar to DPPM, IDPPM and DAPPM. An example of OFAM-1D symbol structure is shown in Fig. 2 for source bits $M = 2$ and $n = 2$, where four "0" bits ($N_0 = 4$) are needed before the DAPPM symbols. Although OFAM-1D has more average bit length than OOK, it can produce a higher bit-rate because the laser repetition rate is not limited. The bit-rate of OFAM-1D is calculated by,

$$B_{OFAM-1D} = \frac{2 \times M \times R_L}{2N_0 + 1 + (2^M/n)} \quad (15)$$

The data rate of OFAM-1D can be higher than other techniques, even at a lower repetition rate if a probability-based symbol mapping is considered, where the OFAM-1D symbols with the lowest number of bits are associated with symbols with the highest probability of occurrence. If "0" and "1" bit occurrence probability is the same in OOK symbols, the power efficiency of the OFAM-1D with respect to OOK is,

$$P_{OFAM-1D/OOK} = \left(1 + \frac{M-2}{M}\right) \times 100\% \quad (16)$$

Equation (16) is the same as (13) because OFAM-1D also has only one "on" chip in each symbol. Although the amplitude is varied, similar to DAPPM, in OFAM-1D the laser pulse energy is the same where the EFTL lens changes laser irradiance in the focal spot. Therefore, OFAM-1D is more

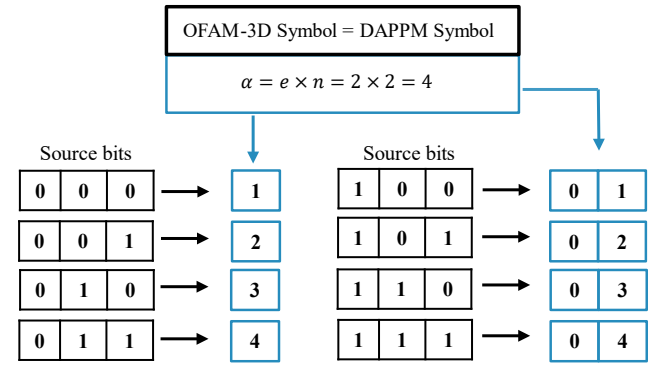


Fig. 3. Illustrating the OFAM-3D symbol structure with an example for $M = 3$, $e = 2$ and $n = 2$.

power efficient than OOK for $M > 2$, similar to PPM, DPPM, and IDPPM.

B. Dynamic Focusing Position (OFAM-3D)

OFAM-1D targets focal points at different depths (z -axis) to vary the shape of the generated plasma and consequently the acoustic pressure. The OFAM-3D variant is designed to avoid vapor cloud formation by transmitting laser pulses to different focal points on the x - y plane. The idea is to preclude vapor cloud formation by maintaining a minimum distance (d_v) between two adjacent focal points and avoiding laser transmission in the same location before T_v time. Therefore, the N_0 bits required for VCD in OFAM-1D technique can be excluded and only DAPPM symbols can be used for data transmission. Fig. 1(b) illustrates the OFAM-3D technique for $n = 2$ using an EFTL lens similar to OFAM-1D but rotating the laser to create focal points in different locations on a circular shaped base. There can be a total of n number of bases depending on the total focal lengths. In the example, five different focal points are on each base (Base-1 and Base- n) because five steps per full circular rotation are considered. For the longer focal length (f_1), the focal points are B_{11} to B_{15} and for the shorter focal length (f_n), the focal points are B_{n1} to B_{n5} . It is worth noting that the number of focal points on deeper bases can be larger because of the bigger radius and consequently the covered area.

In OFAM-3D, the laser source can rotate using a stepper motor in a fixed direction only to transmit a beam; thus, the present focal point is dependent on the previous focal point. For example, if the last focal point was B_{11} or B_{n1} , then the laser will rotate a step for the next laser beam transmission and the focal point will be either B_{12} or B_{n2} depending on the focal length. In the bottom right side of Fig. 2(b), the operation of the OFAM-3D technique is illustrated as a right circular cone. The position of the laser transmitter with EFTL lens is considered at position A and is tilted at θ_c degree from the norm on the water surface AH . For each laser pulse transmission, the laser will rotate \emptyset degree and transmit to a different point on the perimeter of the bases. D is the center of the Base- n and the angle created at the center of the base per step laser rotation is θ_m . Here, AFG is the largest and ABC is the smallest right circular cone created by the f_1 and f_n , respectively. Thus, for the ABC cone, slant height is $AB = AE = f_n$. The height from vertex A to Base- n is $AD = h_n$, the radius of Base- n is $BD = r_n$, and the semi-vertical angle of the cone is θ_c . B and E are the two adjacent focal points where the angle between BD and ED is θ_m . The distance between B and E is d_n and d_n should be $\geq d_v$ to mitigate the vapor cloud effect. The height from the EFTL lens

to any base depends on the focal length and laser tilt angle and can be measured by,

$$h_n = f_n \cos \theta_c \quad (17)$$

The height from the base and the laser tilt angle is inversely correlated for a fixed focal length. However, the radius of a base and laser tilt angle is positively correlated for a fixed focal length,

$$r_n = f_n \sin \theta_c \quad (18)$$

Therefore, the perimeter of a base can be increased by increasing θ_c . The distance between two adjacent focal points, i.e., length of the chord, can be determined from the triangle *BAE* using the law of cosines,

$$d_n = \sqrt{f_n^2 + f_n^2 - 2f_n f_n \cos \emptyset} = f_n \sqrt{2(1 - \cos \emptyset)} \quad (19)$$

Similarly, from the triangle *BDE*,

$$d_n = r_n \sqrt{2(1 - \cos \theta_m)} \quad (20)$$

Thus, the distance d_n can be increased by increasing \emptyset and θ_m and should avoid the vapor cloud effect if $d_n \geq d_v$. However, increasing d_n will decrease the total number of focal points (m) on the perimeter of a base. m can be calculated by dividing the total angle of the circular base, which is 360° by the per step rotation angle created at the center of the base (θ_m). Thus, $m = \frac{360^\circ}{\theta_m}$ and substituting θ_m from (20),

$$m = \frac{360^\circ}{\cos^{-1} \left(1 - \frac{d_n^2}{2r_n^2} \right)} \quad (21)$$

Therefore, the laser repetition rate depends on m because we are considering circular rotation and want to give at least T_v time delay before transmitting the laser to the same focal point. Thus, the relation between laser repetition rate (R_L) and m is,

$$R_L \leq m \times R_{max} \quad (22)$$

Therefore, the laser repetition rate can be increased by raising the value of m , which will increase the data rate. In OFAM-3D, the data rate can be increased even more by combining different focusing and laser pulse energy to create various laser irradiance in the underwater focal point. This can create even more different plasma shapes and volumes to generate acoustic signals with different patterns. However, using a single laser transmitter to generate varying laser pulse energy during data transmission is challenging. Therefore, we use a round, step-variable neutral density (ND) filter with multiple sections with different optical densities (ODs) [61]. The OD values indicate the attenuation factor provided by the ND filter and related to transmission (T), where $T = 10^{-OD}$. Therefore, the section with a larger OD will reduce laser pulse energy more. The number of sections with different ODs will depend on the total number of energy levels (e) that one wants to transmit.

Two stepper motors are required on the transmitter side of OFAM-3D. One is for rotating the ND filter to vary the laser pulse energy and another is to rotate the whole laser to transmit to different locations. The laser modulator and EFTL lens will work based on the data similar to the OFAM-1D technique. There can be $(e \times n) + 1$ different bits generated by OFAM-

3D. Here, one is added to include the "0" bit where no laser beam will be transmitted. Thus, the total non-zero bits equals to $e \times n$, which can be generated using different combinations of energy levels $\{E_1, E_2, \dots, E_e\}$ and focal lengths $\{f_1, f_2, \dots, f_n\}$. For example, if $e = 2$ and $n = 2$, there will be a total of four non-zero bits ("1" bit, "2" bit, "3" bit and "4" bit). In such a case, data = "1" bit means E_1 laser pulse energy will be focused with f_1 focal length. Similarly, data = "2" bit means the combination of E_2 with f_1 , data = "3" bit means the combination of E_1 with f_2 and data = "4" bit means the combination of E_2 with f_2 . An UWN will receive only one acoustic signal for each symbol; demodulation can be done by comparing the received signal's pressure with threshold values and total delay before receiving the signal, similar to the OFAM-1D. Demodulation considering only received acoustic peak-peak pressure should achieve good BER for lower order OFAM, where $n = 2$ and $e = 1$. The demodulation technique for higher order OFAM is discussed in the next subsection.

OFAM-3D symbols also have unequal durations and do not require symbol synchronization, similar to OFAM-1D, DPPM, IDPPM and DAPPM. An example of OFAM-3D symbol structure is shown in Fig. 3 for source bits $M = 3$, $e = 2$, $n = 2$. We can observe that the OFAM-3D symbols are the same as the DAPPM symbols if $\alpha = e \times n$. The bit-rate of OFAM-3D can be calculated by,

$$B_{OFAM-3D} = \frac{2(e \times n) \times M \times R_L}{2^M + (e \times n)} \quad (23)$$

The average bit length per symbol for OFAM-3D decreases with the increase in e and/or n . Therefore, OFAM-3D can be tuned to boost the data rate. The repetition rate of the laser can also grow up to $m \times R_{max}$ to increase the data rate. OFAM-3D uses a fixed laser pulse energy, although the irradiance in the focal point varies due to the different energy and focal length created by the ND filter and EFTL lens, respectively. If "0" and "1" bit occurrence probability is the same as in OOK, and the same laser pulse energy is required to transmit a non-zero bit for both OOK and OFAM-3D, then the power efficiency of the OFAM-3D relative to OOK will be,

$$P_{OFAM-3D/OOK} = \left(1 + \frac{M-2}{M} \right) \times 100\% \quad (24)$$

The OFAM-3D becomes more power efficient than OOK as M grows and achieves the same efficiency as OFAM-1D, PPM, DPPM, and IDPPM.

C. Machine Learning-based Demodulation

Higher-order OFAM can transmit more distinct bits by generating different acoustic signals to increase the data rate. For example, with $n > 2$ in OFAM-1D and $e \times n > 2$ in OFAM-3D more than two different acoustic signals can be generated. However, demodulation with low BER can be challenging in complex underwater environments for higher-order OFAM, where UWN is required to compare the received signals with more than two threshold values. Moreover, there is a possibility of generating similar peak-peak acoustic pressure by two different laser modulation parameters. For example, peak-peak acoustic pressure generated by laser pulse energy E and with focusing length f can be the same as laser pulse energy $4 \times E$ and with focusing length $2 \times f$ combination because they will create the same irradiance in the focal spot. Therefore, the demodulation by the received acoustic signal's strength

compared with threshold values may not achieve a robust long distance communication link. Moreover, water stratification, different temperatures, and salinity levels influence acoustic signal propagation underwater. We tackle these issues by using ML-based demodulation for higher order OFAM.

In OFAM, the laser modulation parameters are the pulse energy and focusing geometry. Correspondingly, the characteristics of the generated acoustic signals depend on these laser parameters, as discussed in Section III. For instance, the generated acoustic signal contains breakdown and bubble collapse shockwaves where the shockwaves amplitude, number of bubble-generated acoustic transients, and signal directionality depend on the laser pulse energy and focusing geometry. Moreover, the acoustic spectrum is complicated because of the frequency components associated with bubble oscillation, especially the delay between the initial shockwave and the adjacent bubble-generated acoustic transients, which produce a modulation of the frequency content [24]. Thus, the acoustic signal's frequency pattern also changes in addition to the time domain pattern when the laser pulse energy and focusing are varied during OFAM modulation. Therefore, a ML model can recognize these patterns of the generated acoustic signal based on both time and frequency domain features and classify the signals accordingly. Demodulation considering both time and frequency domain should increase the demodulation accuracy because the frequency domain should be distinctive even if the observed peak-peak acoustic pressures are not distinct enough.

An underwater acoustic signal experiences one of the harshest propagation environments. Therefore, researchers have recently considered the use of ML techniques for underwater channel modeling, adaptive modulation and acoustic data classification and demodulation in underwater acoustic communication [62]–[67]. In optoacoustic communications, ML models can learn the generated acoustic signals patterns by training with data generated using different laser modulation parameters; the trained ML model can then be employed to classify the received signal to conduct demodulation. A training dataset containing the acoustic signals labeled with corresponding laser modulation parameters is required to train a model. There are several ways to derive information from raw optoacoustic signals. We can summarize the fundamental steps for ML-based demodulation as: collection of raw optoacoustic data, preprocessing of the raw acoustic data, segmentation, extracting features and signal classification for demodulation. Fig. 4 represents a general structure of our ML-based demodulation method.

Data Acquisition and Preprocessing: There are no large number of optoacoustic signal generation data available in literature that can be used to train ML models. Moreover, the optoacoustic process can generate an anisotropic signal specially for elongated plasma shapes, as discussed in Section III. Thus, the dataset should contain the received acoustic signals from different directions relative to the laser beam axis. Therefore, we constructed a dataset by collecting the experiment results in our laboratory. The dataset containing different laser modulation parameters and the underwater receiver positions are discussed in detail in the next section. The raw signals should be preprocessed before the training stage and the very first step of preprocessing should be noise filtering. Additionally, high-frequency acoustic signals cannot propagate long distances in water because of the high absorption coefficient. Therefore, OFAM applies a 3rd order low-pass filter

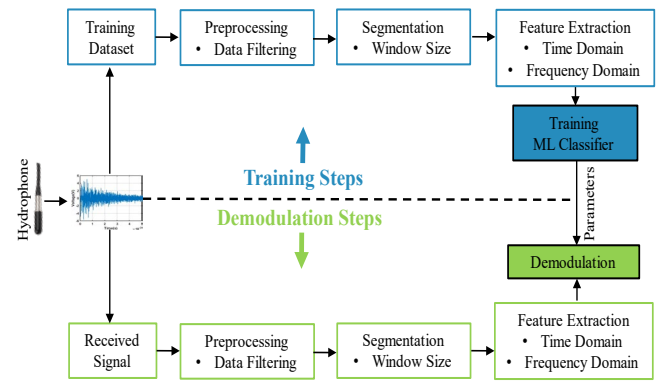


Fig. 4. Outlining the training and demodulation steps in ML-based OFAM.

with a 200 kHz cut-off frequency to remove the high frequencies. We carefully select the filter parameters, i.e., cut-off frequency and filter order to avoid introducing any undesired delay into the filtered data.

Segmentation and Feature Extraction: The window size is subject to trade-off between two perspectives: information and resolution. Generally, the window size should be the same as the bit duration and include all the acoustic transients generated from a single laser pulse. Then, features are extracted from this window. The most crucial step before classification is to extract useful and distinct information from the data [68]. The time domain features can be extracted directly from the received data. The Fast Fourier Transform (FFT) is broadly used to obtain the signal's frequency domain to extract frequency domain features. Examples of features that can be extracted from the time domain are: mean, standard deviation (SD), variance, root mean square (RMS), mean absolute deviation (MAD), maximum value, minimum value, peak-peak pressure, skewness, kurtosis and energy. Similarly, frequency domain features are: mean, SD, variance, MAD, peak amplitude, peak frequency, skewness, kurtosis and energy. Next, we identify relevant features for the classification. The importance of feature selection has four key factors: to make the model simpler by lowering the number of parameters, to speed up training, to lessen overfitting by boosting generalization, and to avoid the curse of dimensionality [69]. Thus, the selection of relevant features can increase the demodulation accuracy.

Demodulation: The last step is training the ML classifier using the relevant time and frequency domain features. The best-performing ML classifier in this method is discussed in the validation section. Finally, this trained ML model can classify the unlabeled received acoustic signals for demodulation. The UWN will follow the same steps mentioned above for received signals during optoacoustic communication and use the trained ML model for signal demodulation.

VI. PERFORMANCE ANALYSIS

A laboratory experiment has been conducted to analyze the nonlinear optoacoustic signal generation using different modulation techniques and compare the performance to OFAM. First, we discuss the experimental setup and the laboratory findings. Then, we simulate the data rate, power efficiency and BER based on laboratory results. Finally, the performance of ML-based demodulation is validated and compared with the peak detection based technique of [56], which is referred to as PDOOK when showing the results.

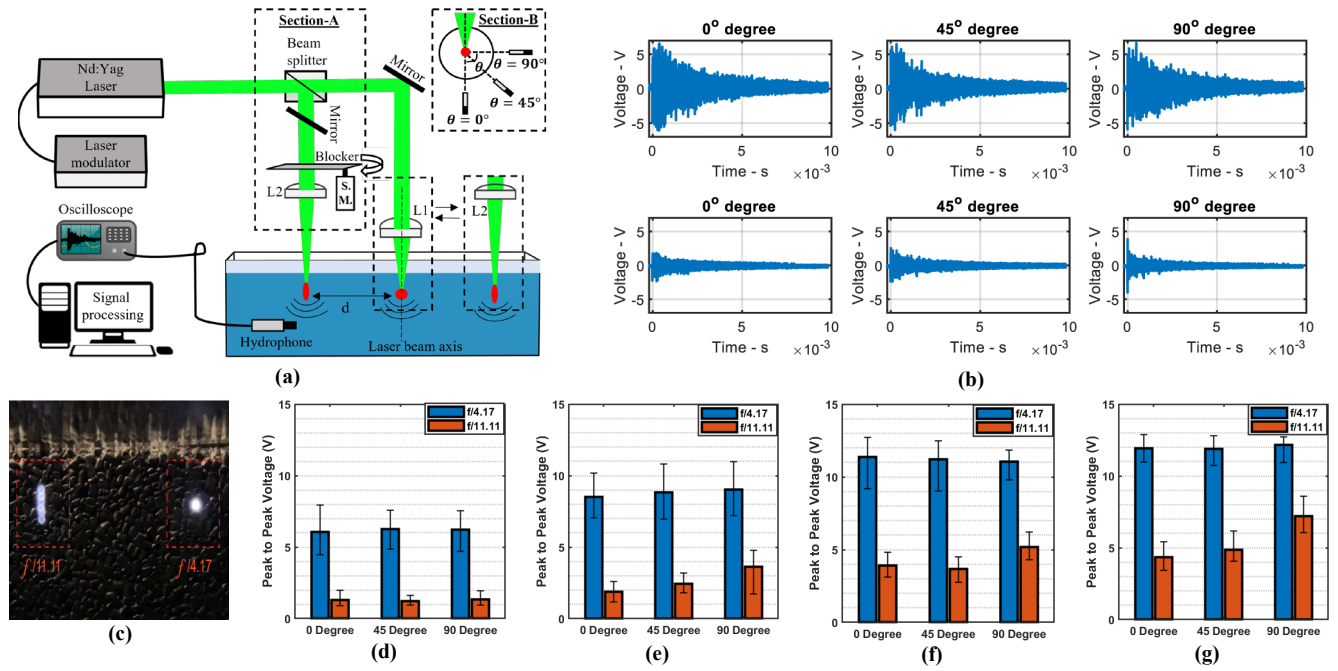


Fig. 5. (a) Schematic of the experimental setup used to measure optoacoustic signal. (b) Generated acoustic signal in 0°, 45° and 90° respect to the laser beam axis using 60 mJ- $f/4.17$ combination (first row) and 60 mJ- $f/11.11$ combination (second row). (c) Multi-core cylindrical shaped weak plasma generated by $f/11.11$ and single-core spherical shaped strong plasma generated by $f/4.17$. Peak-peak voltage of experimentally generated acoustic signal using (d) 22 mJ (e) 35 mJ (f) 50 mJ (g) 60 mJ laser pulse energy. Each presented value is the average of one hundred measurements with error bars showing the maximum and minimum values.

A. Experimental Setup and Results

The schematic of the experimental setup is shown in Fig. 5(a). We have used a Geoscience Laser Altimeter System (GLAS) Q-switched Nd:YAG laser with 6 ns pulses at 1064 nm with a repetition rate up to 40 Hz. The laser beam diameter is 1.8 cm and laser pulses are focused on the water with a 7.5 cm (L1) and a 20 cm (L2) lens. A Xilinx FPGA (Artix-7) is used to generate data bits and connected to the laser to transmit to a 1.27 m (L) \times 0.6 m (W) \times 0.8 m (H) water tank made with glass. To capture the underwater acoustic signal, a TC4041 hydrophone with a frequency range of 15 Hz to 480 kHz was strategically positioned at 0°, 45°, and 90° from the laser beam axis. We have observed that the tight focusing with $f/4.17$ creates a compact single core plasma with stronger acoustic emissions, as shown in Fig. 6(b) and 6(c). However, loose focusing with $f/11.11$ creates multiple plasma cores with weaker acoustic emissions, as also noted in [52]. We varied the laser pulse energy and transmitted the laser beam with four different energy levels: 22 mJ, 35 mJ, 50 mJ and 60 mJ. The irradiance in the focal area is calculated using (4) and is shown in Table II. We have successfully generated two different peak-peak pressures by varying the focal length of the lens for each laser pulse energy, as shown in Fig. 5(d)-(g).

TABLE II The laser irradiance in the focal spot for 22 mJ, 35 mJ, 50 mJ and 65 mJ pulse energy focused with 7.5 cm and 20 cm lens.

Laser Pulse Energy	22 mJ	35 mJ	50 mJ	60 mJ
Irradiance (I) for $f/4.17 \times 10^{12}$ W/cm ²	14.6	23.3	33.3	39.95
Irradiance (I) for $f/11.11 \times 10^{12}$ W/cm ²	2.06	3.28	4.68	5.62

We can observe that a single stable spherical-shaped plasma created by $f/4.17$ generates almost similar acoustic pressures in all directions. However, the plasma shape becomes more

elongated as the laser pulse energy increases for laser focusing with $f/11.11$. Consequently, anisotropic acoustic pressure generates where pressure increases from 0° to 90° direction. This directive nature poses demodulation challenges, especially for mobile underwater receivers that rely solely on peak pressure for modulation. It is worth noting that the multipath effect is more severe in our small tanks than real-world settings due to signal reflections with high amplitude from the boundaries. Consequently, the captured acoustic signal significantly distorts due to echoes and reverberations. Thus, we are validating the robustness of our OFAM techniques under the most challenging conditions.

We have done experiments by varying the laser repetition rate and moving the focal point to avoid the vapor cloud effect. R_{max} is found to be 16 Hz, where no acoustic signal is missing for continuous "1" bit transmission. The vapor cloud effect is seen beyond 16 Hz repetition rate, where we start observing missed acoustic signals. Thus, T_v is 62.5 ms in our laboratory setup. In Fig. 6(c), an acoustic signal is missing at a 17 Hz repetition rate. Therefore, the maximum repetition rate for OOK, DPPM, and DAPPM is 16 Hz. As expected, the maximum repetition rate of IDPPM is found to be 32 Hz for the repetitive "01" bit sequence, which is twice R_{max} . The worst bit sequence scenario in PPM is "11000"; we have transmitted the repetitive "11000" bit sequence at 40 Hz, where no acoustic signal is missing, as shown in Fig. 6(d). There is a possibility that PPM can be used with a higher repetition rate for the larger values of M because the "0" bits in PPM symbols work as a delay to mitigate the vapor cloud generated by two consecutive "1" bits. The number of "0" bits required for VCD at 40 Hz for the OFAM-ID technique is two and we have validated the OFAM-ID symbol transmission with a repetitive "001" bit sequence, which is the worst bit sequence of OFAM-ID, as shown in Fig. 6(e).

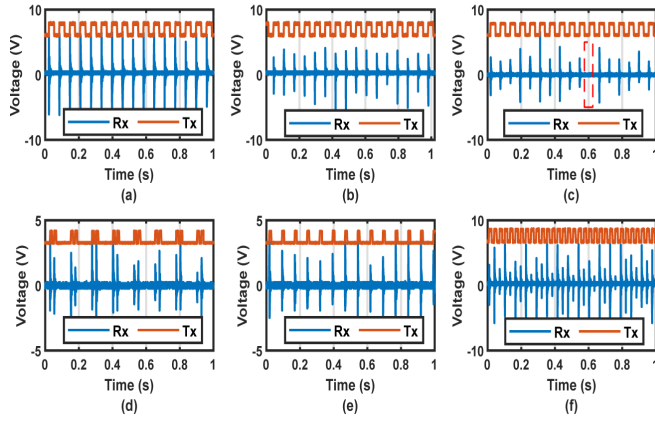


Fig. 6. Experimental optoacoustic signal generation by varying the laser repetition rate up to 40 Hz. The maximum repetition rate is 16 Hz to transmit continuous "1" bit where no vapor cloud effect is observed using (a) $f/4.17$ (b) $f/11.11$. (c) The acoustic signal starts to be missed at 17 Hz, marked with a dashed rectangle, due to vapor cloud formation. The continuous acoustic signal is generated using (d) "11000" repetitive bit sequence in 40 Hz for PPM technique, and (e) "001" repetitive bit sequence in 40 Hz for OFAM-1D technique. (f) The signals generated by OFAM-3D for $e = 1$, $n = 2$ using 32 Hz.

In order to demonstrate OFAM-3D technique, we have used a beam splitter to make two laser beams and focused them in water to determine the minimum distance (d_n) between two focal points to preclude the vapor cloud effect. A stepper motor with a beam blocker is used to rotate continuously to block one beam and allow the other beam, as shown in Section-A of Fig. 5(a). We have used $f/4.17$ and $f/11.11$ in two positions. Based on (22), the maximum repetition rate is 32 Hz for OFAM-3D with $m = 2$ and $R_{max} = 16$ Hz. When transmitting continuous "1" bits at 32 Hz, we observed no missed acoustic signal for $d_n = 2.5$ cm, as shown in Fig. 6(f). Alternating high and low peak-to-peak signals were observed because focusing the laser beam using $f/4.17$ generates stronger signals. Meanwhile, weaker signals are generated when the laser beam is focused using $f/11.11$. Hence, the minimum distance required to avoid the vapor cloud effect is $d_v \geq 2.5$ cm in our laboratory conditions. Thus, OFAM-3D can prevent the vapor cloud effect by moving the focal point only 2.5 cm away from the previous focal point. Therefore, OFAM-3D can transmit data using a high repetition rate depending on the m value to boost the data rate. We note that, T_v and d_v can vary for plasmas generated with different laser parameters.

B. Data Rate and Power Efficiency

We have also measured the bit rate of OFAM and compared it with PDOOK [56], which is developed based on OOK. Moreover, OFAM is compared with other popular modulation techniques: PPM, DPPM, IDPPM, DAPPM and the results are shown in Fig. 7(a)-(b). We have considered two cases; in the first case, shown in Fig. 7(a), a stationary laser with a fixed focusing position is considered for all techniques. Therefore, the maximum repetition rate of the PDOOK, PPM, DPPM, IDPPM and DAPPM is 16 Hz, 40 Hz, 16 Hz, 32 and 16 Hz, respectively. In the second case, shown in Fig. 7(b), dynamic laser focusing is considered for all the traditional techniques, i.e., similar to OFAM-3D, in order to mitigate vapor cloud formation. Although the vapor cloud effect does not limit the repetition rate for OFAM, we have simulated up to 320 Hz. The considered EFTL lenses have a settling time of 15 ms, which can be further reduced to approximately 3 ms by using sparse optimization [70]. In Fig. 7(a), we can observe that OFAM-1D achieves a higher bit-rate than all traditional modulation techniques for only $n = 2$ and $R_L = 320$ Hz. The bit-rate of OFAM-1D can further grow by increasing n and R_L . All other techniques have a limited bit-rate because of the laser repetition rate constraint that is imposed to mitigate the vapor cloud effect.

In Fig. 7(b), all the traditional techniques are also considered using the 320 Hz repetition rate. In such a case, the bit-rate of DAPPM and OFAM-3D should be the same if $\alpha = e \times n$. Therefore, the bit-rate of OFAM-3D for $e = 1$ and $n = 2$ should be similar to that of DAPPM for $\alpha = 2$, shown in Fig. 7(b). Meanwhile, OFAM-3D with $e = 4$ and $n = 2$ yields a higher bit-rate than all other techniques up to $M = 6$. PDOOK could provide the best performance for $M = 7$ and 8, because the average bit per symbol increases with the higher value of M , consequently the bit-rate of PDOOK stays constant while the bit-rate of other techniques diminishes. However, the data rate of OFAM-3D can be higher than other techniques if a probability-based symbol mapping is applied. Fig. 7(c) compares the power efficiency of the different modulation techniques relative to PDOOK. Here, power efficiency of 100% means that the modulation technique matches the power efficiency of PDOOK. The relative power efficiency to PDOOK remains the same for all other techniques, except DAPPM. This is consistent with (13), (16) and (24). We can observe that DAPPM has lower power efficiency than PDOOK for lower M values and also power efficiency decreases if α increases, as also implied by (14).

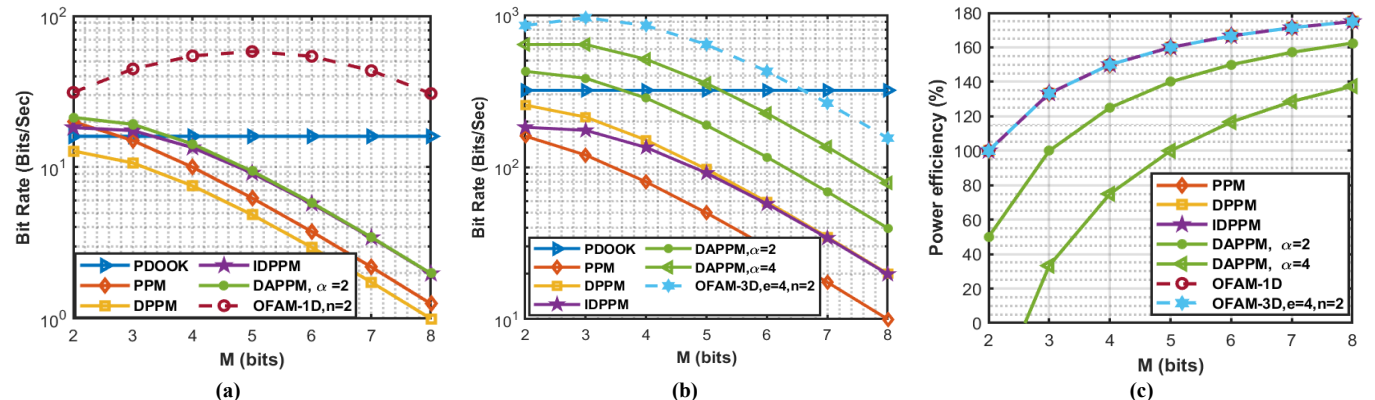


Fig. 7. The bit-rate for different modulation techniques for optoacoustic communication using (a) a stationary laser with a fixed focusing position (b) dynamic focusing to move the focal point. (c) Power efficiency relative to PDOOK for different modulation techniques.

TABLE III Frequency of some ASCII characters in a novel and their corresponding symbol mapping for different modulation techniques.

[illegible]

To better assess the performance of OFAM, we have conducted simulation of text communication using the ASCII characters of a novel written by William Morris entitled: "The Well at the World's End". The novel is provided in a text file of size 1.186 MB taken from the Gutenberg Project [71]. In Table III, the probabilities for the ASCII characters were obtained by computing the occurrences of the characters in the text file (not all of them are shown in the table). The symbol mapping is done based on the probability to achieve the highest data rate, where the symbols with the lowest number of bits are assigned to the characters with the largest frequency of appearance in the text. We have also considered both fixed and dynamic laser focusing, as shown in Fig. 8(a)-(b), respectively, and simulated up to 320 Hz. In both cases, OFAM achieves the highest symbol rate even for $M = 7$. PPM yields the second-highest symbol rate for the fixed focal point case in Fig. 8(a); yet it has the lowest symbol rate for the dynamic focal point case in Fig. 8(b). Based on [24], we have considered that PPM uses the 320 Hz repetition rate for both cases because the experimental results show that three consecutive "1" bits are required to create the vapor cloud effect at 500 Hz. Therefore, all the "0" bits in the PPM symbols can be utilized as a vapor cloud delay and the symbol rate is the same for both cases. The DAPPM technique achieves the second highest symbol rate for $\alpha = 4$, but requires four laser transmitters to support four different pulse energy levels. In the fixed focusing case, the data rate of PDOOK and

OFAM-1D with $n = 2$ is 15.96 (2.28×7) bits/sec and 95.55 (13.65×7) bits/sec, respectively, for $M = 7$. Similarly, in the dynamic focusing case, the data rate of PDOOK and OFAM-3D with $e = 4$ and $n = 2$ is 319.9 (45.7×7) bits/sec and 1409.8 (201.4×7) bits/sec, respectively. Thus, OFAM-1D and OFAM-3D could achieve approximately 6 times and 4.4 times higher data rates than PDOOK. Moreover, Increasing the laser modulation parameter n and/or e can boost the data rate of OFAM-1D and OFAM-3D. Additionally, as the settling time of the EFTL lenses improves with future technological advancements, the data rates of OFAM are expected to see even greater increases. Fig. 8(c) illustrates the power efficiency where with the exception of DAPPM, all techniques achieve 137% power efficiency relative to PDOOK. For $\alpha = 2$, DAPPM shows 110% power efficiency, but DAPPM underperforms PDOOK for $\alpha = 4$.

OFAM-1D is an ideal choice for application scenarios that require moderate data rates, such as environmental monitoring or basic command and control messages that need to be transmitted from air to underwater nodes. These scenarios benefit from a straightforward modulation approach where a lower data rate suffices. In contrast, OFAM-3D intentionally embraces complexity to achieve high data rates and power efficiency simultaneously. It is specifically designed for demanding applications such as transmitting high-resolution, real-time images in underwater environments.

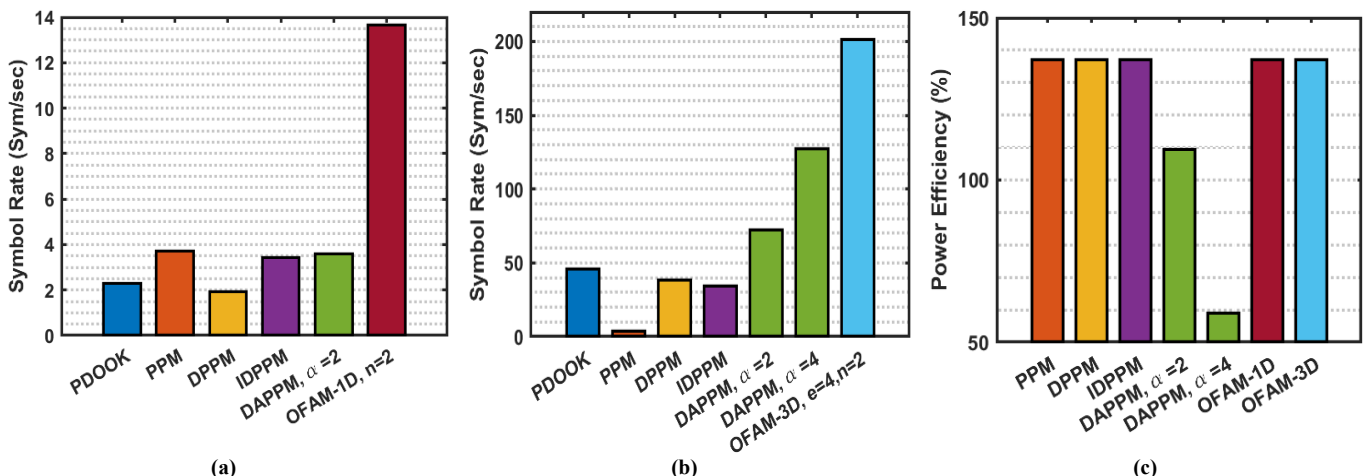


Fig. 8. The symbol rate of the different modulation techniques based on the mapping in Table 3 while using (a) stationary focusing, (b) dynamic focusing to move the focal point, and (c) power efficiency increases relative to PDOOK.

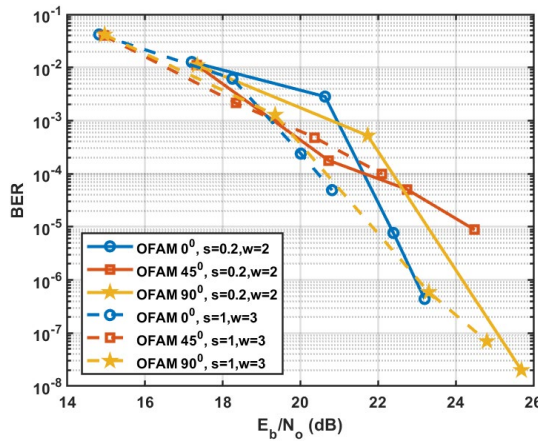


Fig. 9. BER of third order OFAM for different ambient noise levels at a 300m distance from the acoustic source, and 0°, 45° and 90° receiver positions relative to the laser beam propagation.

C. BER Simulation

To evaluate the underwater communication range, we have simulated the BER of OFAM in MATLAB for different underwater depths and UWN positions using our experimental results. We have considered a third order setting ("0" bit, "1" bit and "2" bit), i.e., $n = 2$ for OFAM-1D and $e = 1$ and $n = 2$ for OFAM-3D. The peak-peak pressure generated by $f/4.17$ is mapped with "2" bit, the peak-peak pressure generated by $f/11.11$ is mapped with "1" bit and "0" bit means no signal is transmitted. The SL values are based on our experimental results and shown in Fig. 5(d)-(g). The sound intensity level received by the UWN at a certain underwater distance from the acoustic source plasma is determined as specified in Appendix A. At the beginning of the transmission, 64 control bits are transmitted to the UWN to calculate the two signal pressure thresholds for demodulation and then 10^5 data bits are transmitted. Fig. 9 shows the BER at 300 m underwater depth using our experimental SL values while considering the underwater ambient noise discussed in Appendix B. We have varied the wind speed and shipping activity values to vary the ambient noise level. As expected, BER grows for higher ambient noises; better BER is experienced in the 90° direction because of the greater SL values. We observe that BER decreases as the signal-to-noise per bit increases; the latter generally grows with the increase in laser pulse energy. This relationship suggests that the achievable bit rate leaps with

higher laser beam power. We also note that OFAM can achieve low BER even at a 300 m depth for 50 mJ and 60 mJ laser pulse energy. This transmission range can be increased or BER can be reduced by using higher laser pulse energy to boost the SL. Consequently, fine-tuning the laser pulse energy is critical in achieving specific transmission ranges or BER targets in practical implementations.

D. ML-based Demodulation Validation

We have conducted experiments to assess the performance of ML-based demodulation for transmissions in higher-order OFAM and compare it with PDOOK [56]. We have constructed a dataset for training-testing by collecting 2400 acoustic signals in our laboratory, as shown in Fig. 10(a). Each data file contains a matrix of size 10^6 rows \times 2 columns and corresponds to one 10 ms recording at the sample rate of 10^8 Hz. There are 8 labels in the dataset combining four laser pulse energy and two focusing lenses where the labels represent data bits. From an ML point of view, the primary goal of this experiment is to correctly classify these 8 labels.

The dataset is divided into three parts based on the underwater receiver position relative to the laser beam incident. First, each data item is passed through a 3rd order Butterworth low-pass filter with a cut-off frequency of 200 kHz to remove the high frequencies; then a window of size in (0, 5] ms is selected from the filtered data, as shown in Fig. 10(b). Both time and frequency domain features mentioned in Section V are extracted for training the classifiers. We have used the most common and widely explored classifiers, namely, Decision Tree (DT), K-Nearest Neighbors (KNN), Linear Discriminant Analysis (LDA), Logistic Regression (LR), Support Vectors Machine (SVM) and Random Forest (RF) [66]-[69],[72][73]. The performance of the classifiers is evaluated with 5-fold cross-validation. The data is randomly partitioned into five subsets, four of which are treated as training data and the remaining subset is used for testing. The cross-validation process is repeated 5 times and the estimated accuracy of the classifier is averaged as shown Fig. 10(c). To understand the best position of the UWN relative to the laser beam incident, we have checked the accuracy by cross-validation based on the data of the 0°, 45° and 90° UWN positions. Then, the model accuracy is checked for any position of the UWN, while considering the data of all receiver's positions. In our experiments, RMS (time), MAD (time), skewness (frequency) and kurtosis (frequency) are found less important features for classification and got higher accuracy after removing them.

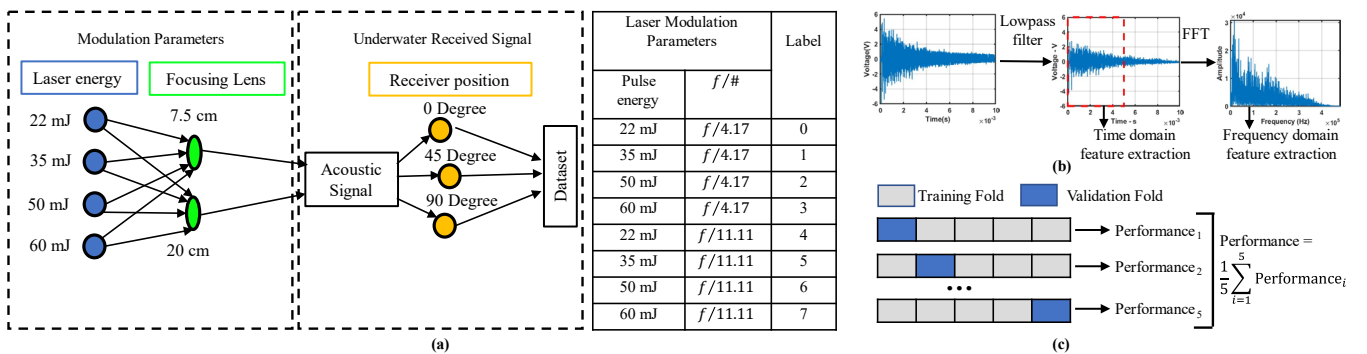


Fig. 10. (a) Schematic of the generation of the dataset and the labels of the different laser modulation parameters (b) Data preprocessing by selecting a 5 ms window and applying a low-pass filter. Then features are extracted from the time and frequency domains. (c) 5-fold validation by randomly partitioning the dataset into five subsets, four of which are treated as training data and the remaining one for testing. This process is repeated 5 times and the performance of the classifier is determined by averaging the five performances.

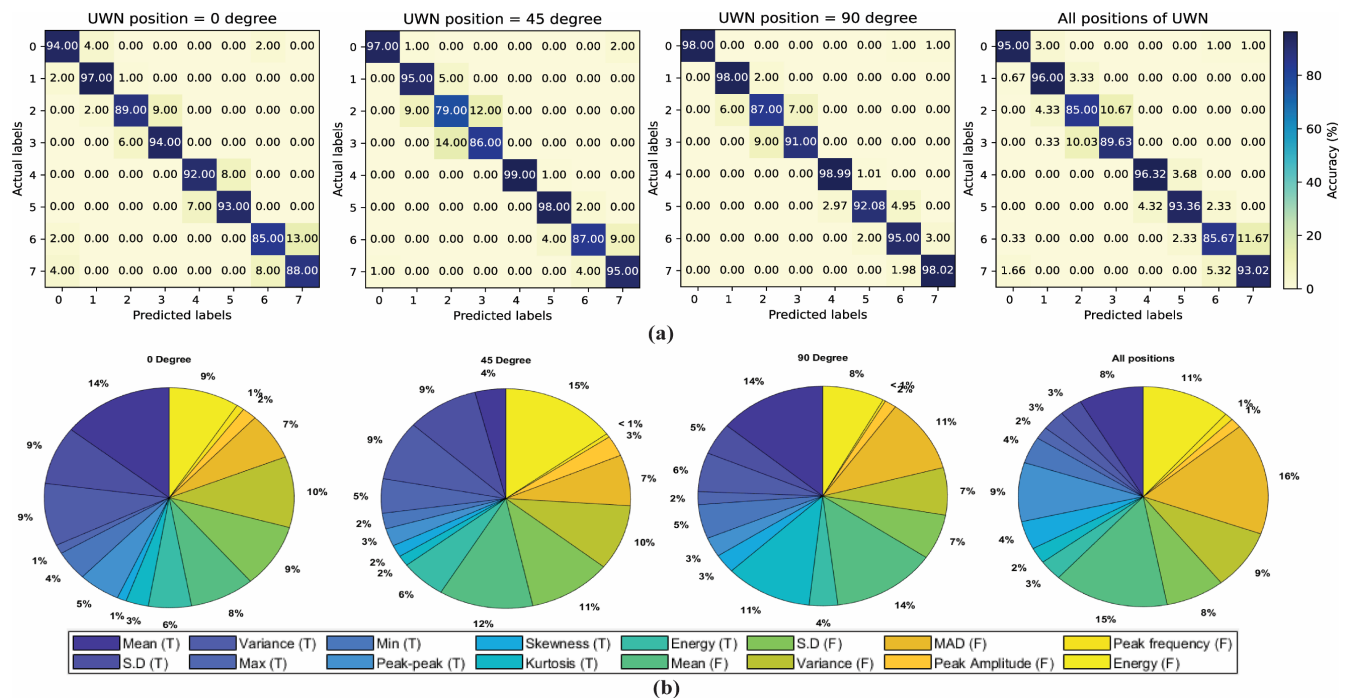


Fig. 11. (a) Confusion matrix depicting the accuracy of the RF model considering different UWN positions and data for all positions. (b) Feature importance in the RF model for classification.

Among the classifiers, RF achieved the highest accuracy in all cases, as depicted using the confusion matrix in Fig. 11(a). The best position of UWN is found to be at 90° relative to the laser beam, where the highest accuracy of 94.75% is achieved. The second best position is 45° with 92% accuracy and the lowest accuracy of 91.5% achieved in the 0° direction. The accuracy when considering all UWN positions is 91.75% using RF. The feature relevance to the classification using RF is reported in Fig. 11(b), where the mean (time domain) and energy (frequency domain) are found to be the most important in the 0° and 45° directions, respectively. In the 90° direction, the mean happens to be the most relevant frequency domain feature. When considering all positions, MAD is the most critical feature. Therefore, both time and frequency domain features are essential to achieve high accuracy for higher-order OFAM signal demodulation.

TABLE IV Comparison of demodulation accuracy and inference time among different ML algorithms.

	SVM	KNN	LDA	LR	DT	RF
Demodulation accuracy (%)	83.66	88.37	89.33	70.5	87.37	91.75
Inference time (ms)	0.11	0.45	0.16	0.05	0.04	0.58

Table IV shows the demodulation accuracy using different ML classifiers considering all UWN positions. The analysis includes the inference time for each signal post feature extraction, which requires 7.28 ms on an Intel Core-i7 system with 32 GB RAM. The feature extraction takes longer because

each signal has 50K data points. Notably, Random Forest (RF) exhibited the highest accuracy but also the longest inference time. This increased time for RF can be attributed to its ensemble nature, where multiple decision trees need to be individually processed and their results aggregated. Therefore, when selecting a machine learning algorithm for communication, it is essential to balance accuracy with total demodulation time, ensuring it remains below the bit duration to facilitate effective real-time processing.

The performance of ML-based demodulation technique using RF is compared with that of PDOOK [56] in Table V. The results are the average for any UWN position. The thresholds for the peak detection-based demodulation method, i.e., PDOOK, are calculated from 128 pilot symbols. PDOOK achieves poor performance because the peak pressure values are very close and are sensitive to signal directionality, as observed in Fig. 5(d)-(g). Therefore, demodulation based on the received peak pressure proves insufficient for robust demodulation in higher-order OFAM systems. Although the peak detection-based demodulation requires less inference time, it could yield only 66.86% accuracy, which is way less than the 91.75% accuracy achieved by ML-based demodulation. Hardware-based implementation, e.g., using FPGA platforms, and refining the model refinement through pruning and focused feature selection are effective strategies for enhancing the response time of ML-based demodulation in practice. Further, incorporating high-level synthesis tools can optimize the system, ensuring a faster and more efficient output, ideal for real-time applications.

TABLE V Comparing the performance of ML-based demodulation of OFAM (using RF) to that of PDOOK for any UWN position.

	Overall Accuracy	Label-1	Label-2	Label-3	Label-4	Label-5	Label-6	Label-7	Label-8	Inference Time
Peak detection-based demodulation [56]	66.86%	70.86%	92.45%	70.50%	71.58%	100%	50.36%	45.32%	33.81%	0.02 μ s
ML-based demodulation of OFAM using RF	91.75%	95%	96%	85%	89.63%	96.32%	93.36%	85.67%	93.02%	0.58 ms

VII. CONCLUSIONS

For air-water cross-medium communications, the nonlinear optoacoustic process has the ability to address the difficulty of establishing long-haul links. However, the vapor cloud and cavitation bubbles that result from such a process preclude the subsequent generation of acoustic signals, which limits the laser repetition rate and, consequently the achievable bit-rate. This paper has presented OFAM, a modulation technique that avoids the vapor cloud effects. Two configurations are described: a minimum delay between two consecutive laser pulses (OFAM-1D) and transmission of each laser pulse to a different location by rotating the laser focal point (OFAM-3D). OFAM is shown to outperform all the traditional techniques in terms of data rates and power efficiency. Simulation using experimental data indicates that lower order OFAM configurations can achieve great BER even at a 300 m underwater depth. For higher-order OFAM settings, we incorporate ML to demodulate the received acoustic signals. Using time and frequency domain features, Random Forest is found to yield the highest demodulation accuracy. To our knowledge, OFAM is the first technique that supports robust multilevel optoacoustic modulation. Our future work will focus on utilizing deep learning algorithms for channel estimation, equalization, and symbol detection to further elevate the demodulation accuracy in optoacoustic communications.

APPENDIX A: CHARACTERISTICS OF UNDERWATER ACOUSTIC CHANNEL

The acoustic signal strength is weakened during the propagation in the ocean due to the transmission loss (TL). The received sound intensity level (SIL) at a certain distance away from the source can be calculated by,

$$SIL = SL - TL \quad (25)$$

Here SL is the acoustic source level. The attenuation of the acoustic signal is frequency dependent and proportional to the distance between the source and the receiver. TL is mainly caused by spreading and absorption loss, and is given by,

$$TL = 10 \cdot k \log D + (\alpha \cdot D \cdot 10^{-3}) \quad (26)$$

where k , D and α are the spreading factor, distance from the source to the receiver and absorption coefficient, respectively. In Eq. (26), the first part reflects spreading loss and the second part is for absorption loss. The spreading loss is caused by the geometric propagation of acoustic waves away from the source. Spherical and cylindrical spreading models are two simple approximations used to describe the spreading loss. The usual values of k are 2, and 1 for spherical and cylindrical spreading, respectively. An average is typically used, i.e., $k=1.5$. The absorption coefficient (α) in dB/km for frequencies between 100 Hz to 3 kHz is obtained from Thorp's formula [74],

$$\alpha = \frac{0.11 f^2}{1 + f^2} + \frac{44 f^2}{4100 + f^2} + 2.75 \cdot 10^{-4} f^2 + 0.003 \quad (27)$$

Here frequency (f) is in kHz. The α for the frequency range between 3 kHz and 500 kHz can be calculated by Using Schulkin and March model [75],

$$\alpha = 8.68 \cdot 10^3 \left(\frac{SAf_T f^2}{f_T^2 + f^2} + \frac{Bf^2}{f_T} \right) (1 - 6.54 \cdot 10^{-4} P) \quad (28)$$

where $A = 2.34 \times 10^{-6}$ and $B = 3.38 \times 10^{-6}$ are constants, S is the salinity percentage, P (kg/cm²) is the hydrostatic pressure, and f (kHz) is the acoustic wave frequency. The relaxation

frequency f_T (kHz) depends on the water temperature T (°C) and is expressed by,

$$f_T = 21.9 \cdot 10^{6 - 1520/(T+273)} \quad (29)$$

APPENDIX B: UNDERWATER AMBIENT NOISE MODEL

The ambient noise in the ocean can be modeled using four fundamental factors: turbulence (N_t), shipping (N_s), waves (N_w), and thermal (N_{th}) noise. Most of the ambient noise sources can be defined by Gaussian statistics and a continuous power spectral density (PSD) [76]. The following empirical formulas give the PSD of these four noise components in dB re $\mu\text{Pa/Hz}$ as a function of frequency in kHz [77]:

$$10 \log N_t(f) = 17 - 30 \cdot \log f \quad (30)$$

$$10 \log N_s(f) = 40 + 20(s - 0.5) + 26 \log f - 60 \log(f + 0.3) \quad (31)$$

$$10 \log N_w(f) = 50 + 7.5w^{1/2} + 20 \log f - 40 \log(f + 0.4) \quad (32)$$

$$10 \log N_{th}(f) = -15 + 20 \cdot \log f \quad (33)$$

The value shipping activity factor (s) in (31) ranges between 0 and 1 for low to high shipping activity, respectively. The wind speed (w) in (32) is in m/s and N_w is the major factor contributing to the noise in the frequency between 100 Hz and 100 kHz. N_{th} is dominant for frequencies greater than 100 kHz. The PSD of the overall ambient noise in the underwater acoustic channel is given by [76],

$$N(f) = N_t(f) + N_s(f) + N_w(f) + N_{th}(f) \quad (34)$$

The overall noise decays with frequency and the noise PSD decays linearly on the logarithmic scale in certain frequency regions [76].

REFERENCES

- [1] S. A. Mohsan, A. Mazinani, N. Q. Othman, and H. Amjad, "Towards the internet of underwater things: A comprehensive survey," *Earth Science Informatics*, vol. 15, no. 2, pp. 735–764, 2022.
- [2] M. Muzzammil, N. Kouzayha, N. Saeed, T. Y. Al-Naffouri, "Towards Sustainable Internet of Underwater Things: UAV-aided Energy Efficient Wake-up Solutions," pp. 1–7, 2022, *arXiv:2208.12065*.
- [3] M. W. Akhtar, S. A. Hassan, R. Ghaffar, H. Jung, S. Garg, and M. S. Hossain, "The shift to 6G communications: Vision and requirements," *Human-centric Computing and Information Sciences*, vol. 10, no. 1, 2020.
- [4] H. Luo, J. Wang, F. Bu, R. Ruby, K. Wu and Z. Guo, "Recent Progress of Air/Water Cross-Boundary Communications for Underwater Sensor Networks: A Review," in *IEEE Sensors Journal*, vol. 22, no. 9, pp. 8360–8382, 1 May, 2022.
- [5] M. Kong, C. H. Kang, O. Alkhazragi, X. Sun, Y. Guo, M. Sait, J. A. Holguin-Lerma, T. K. Ng, and B. S. Ooi, "Survey of energy-autonomous solar cell receivers for satellite-air-ground-ocean optical wireless communication," *Progress in Quantum Electronics*, vol. 74, p. 100300, 2020.
- [6] E. E. Elsayed, B. B. Yousif, and M. M. Alzalabani, "Performance enhancement of the power penalty in DWDM FSO communication using DPPM and OOK Modulation," *Optical and Quantum Electronics*, vol. 50, no. 7, 2018.
- [7] E. E. Elsayed and B. B. Yousif, "Performance evaluation and enhancement of the modified ook based IM/DD techniques for hybrid fiber/FSO communication over WDM-Pon Systems," *Optical and Quantum Electronics*, vol. 52, no. 9, 2020.
- [8] B. B. Yousif and E. E. Elsayed, "Performance Enhancement of an Orbital-Angular-Momentum-Multiplexed Free-Space Optical Link Under Atmospheric Turbulence Effects Using Spatial-Mode Multiplexing and Hybrid Diversity Based on Adaptive MIMO Equalization," in *IEEE Access*, vol. 7, pp. 84401–84412, 2019.
- [9] E. E. Elsayed, D. Kakati, M. Singh, A. Grover, and G. Anand, "Design and analysis of a dense wavelength-division multiplexed integrated PON-

- FSO system using modified OOK/DPPM modulation schemes over atmospheric turbulences," *Optical and Quantum Electronics*, vol. 54, no. 11, 2022.
- [10] C. Fang, S. Li, Y. Wang, and K. Wang, "High-Speed Underwater Optical Wireless Communication with Advanced Signal Processing Methods Survey," *Photonics*, vol. 10, no. 7, p. 811, Jul. 2023.
 - [11] M. Zhang and H. Zhou, "Real-Time Underwater Wireless Optical Communication System Based on LEDs and Estimation of Maximum Communication Distance," *Sensors*, vol. 23, no. 17, p. 7649, Sep. 2023.
 - [12] W.-S. Tsai, H.-H. Lu, H.-W. Wu, C.-W. Su, and Y.-C. Huang, "A 30 GB/s PAM4 underwater wireless laser transmission system with Optical Beam Reducer/Expander," *Scientific Reports*, vol. 9, no. 1, 2019.
 - [13] M. S. Islam and M. F. Younis, "Analyzing visible light communication through air–water interface," *IEEE Access*, 7, pp. 123830–123845, 2019.
 - [14] H.-H. Lu, C.-Y. Li, X.-H. Huang, P.-S. Chang, Y.-T. Chen, Y.-Y. Lin, C.-X. Liu, and T. Ko, "A 400-GB/s WDM-PAM4 OWC system through the free-space transmission with a water–air–water link," *Scientific Reports*, vol. 11, no. 1, 2021.
 - [15] W.-S. Tsai et al., "500 Gb/s PAM4 FSO-UWOC Convergent System with a R/G/B Five-Wavelength Polarization-Multiplexing Scheme," in *IEEE Access*, vol. 8, pp. 16913–16921, 2020.
 - [16] C. J. Carver et al., "Air-Water Communication and Sensing with Light," *2022 14th International Conference on Communication Systems & NETworks (COMSNETS)*, 2022, pp. 371–374.
 - [17] M. Watson, J.-F. Bousquet, and A. Forget, "Evaluating the feasibility of magnetic induction to cross an air–water boundary," *Int. J. Electron. Commun. Eng.*, vol. 15, no. 6, pp. 262–265, 2021.
 - [18] H. Xu, T. Gu, Y. Zhu, X. Wei, L. Li, and H. Yin, "Communication with a magnetic dipole: Near-field propagation from air to undersea," *IEEE Trans. Antennas Propag.*, vol. 69, no. 2, pp. 1052–1064, Feb. 2021.
 - [19] B. Chai, X. Zhang, and J. Wang, "A Test of Magnetic Induction Communication from Air to Sea," in *2018 OCEANS - MTS/IEEE Kobe Techno-Oceans (OTO)*, pp. 1–4, 2018.
 - [20] Z. Tian, X. Zhang, and H. Wei, "A Test of Cross-border Magnetic Induction Communication from Water to Air," in *2020 IEEE International Conference on Signal Processing, Communications and Computing (ICSPCC)*, pp. 1–4, 2020.
 - [21] X. Wang et al., "Microwave-Induced Thermoacoustic Communications," *IEEE Trans. Microwave Theory Tech.*, vol. 65, no. 9, 2017, pp. 3369–78.
 - [22] M. Mahmud, M. S. Islam, A. Ahmed, M. Younis, and F.-S. Choa, "Cross-medium photoacoustic communications: Challenges, and State of the art," *Sensors*, vol. 22, no. 11, p. 4224, 2022.
 - [23] T. G. Jones, M. Hornstein, A. Ting, D. Gordon and Z. Wilkes, "Characterization of underwater laser acoustic source for navy applications," *2009 IEEE International Conference on Plasma Science - Abstracts*, 2009, pp. 1–1.
 - [24] F. Blackmon and L. Antonelli, "Experimental demonstration of multiple pulse nonlinear optoacoustic signal generation and control," *Appl. Opt.*, vol. 44, no. 1, pp. 103–112, 2005.
 - [25] M. Mahmud, M. Younis, M. S. Islam F.-S. Choa and G. Carter, "Vapor Cloud Delayed-DPPM Modulation Technique for nonlinear Optoacoustic Communication," *Proc. IEEE Global Comm. Conf. (GLOBECOM 2022)*, Rio de Janeiro, Brazil, December 2022.
 - [26] J. M. Kahn and J. R. Barry, "Wireless Infrared Communications," *Proceedings of the IEEE*, Vol. 85, No.2, 265–298, Feb. 1997.
 - [27] M. Mahmud, M. S. Islam, M. Younis and G. Carter, "Optical Focusing-based Adaptive Modulation for Optoacoustic Communication," *Proc. of 30th Wireless and Optical Comm. Conf. (WOCC)*, Taipei, Taiwan, 2021.
 - [28] Q. Shi, Z. He, H. Xu, J. Gao and P. Zhao, "Research on Information Transmission Technology Through the Water–Air Interface Combining a Sonar and a Radar," *IEEE Sensors J.*, 23(7), pp. 7616–7625, 2023.
 - [29] F. Tonolini and F. Adib, "Networking across boundaries: enabling wireless communication through the water–air interface," *Proceedings of the 2018 Conference of the ACM Special Interest Group on Data Communication*, 2018.
 - [30] F. Qu et al., "Cross-Medium Communication Combining Acoustic Wave and Millimeter Wave: Theoretical Channel Model and Experiments," in *IEEE Journal of Oceanic Eng.*, vol. 47, no. 2, pp. 483–492, April 2022.
 - [31] L.-K. Chen, Y. Shao and Y. Di, "Underwater and Water-Air Optical Wireless Communication," in *Journal of Lightwave Technology*, vol. 40, no. 5, pp. 1440–1452, 1 March, 2022.
 - [32] Q. Hu, C. Gong, T. Lin, J. Luo and Z. Xu, "Secrecy Performance Analysis for Water-to-Air Visible Light Communication," in *Journal of Lightwave Technology*, vol. 40, no. 14, pp. 4607–4620, 15 July, 2022.
 - [33] R. Gao, Z. Xu, Y. Ren, L. Song, and C. Liu, "Nonlinear mechanisms in photoacoustics—powerful tools in photoacoustic imaging," *Photoacoustics*, vol. 22, p. 100243, 2021.
 - [34] C. Yang, H. Lan, F. Gao, and F. Gao, "Review of Deep Learning for photoacoustic imaging," *Photoacoustics*, vol. 21, p. 100215, 2021.
 - [35] A. Vogel, J. Noack, G. Hüttman, G. Paltauf, "Mechanism of femtosecond laser nanosurgery of cells and tissues," *Appl. Phys. B*, Vol. 81, 1015–1047, 2005.
 - [36] A. Vogel, K. Nahen, D. Theisen, and J. Noack, "Plasma formation in water by picosecond and nanosecond Nd:YAG laser pulses. I. Optical breakdown at threshold and superthreshold irradiance," *IEEE Journal of Selected Topics in Quantum Electronics*, vol. 2, no. 4, pp. 847–860, 1996.
 - [37] Y. Janapati and P. K. Paturi, "Feasibility of classification of the materials through laser-induced underwater acoustic signatures," *Proceedings of Meetings on Acoustics*, 2021.
 - [38] T. G. Jones, T. C. Yang, S. L. Means, E. R. Franchi, and K. B. Yoo, "Airborne laser-acoustic mine detection system." U.S. Patent 8,228,760, 2012.
 - [39] A. Fitzpatrick, A. Singhvi and A. Arbabian, "An Airborne Sonar System for Underwater Remote Sensing and Imaging," in *IEEE Access*, vol. 8, pp. 189945–189959, 2020.
 - [40] M. Mahmud, M. Younis, G. Carter and F. Choa, "Underwater Node Localization using Optoacoustic Signals," *Proc. IEEE Int'l Conf. on Communications (ICC 2022)*, Seoul, South Korea, May 2022.
 - [41] F. Docchio, P. Regondi, M. R. C. Capon, and J. Mellerio, "Study of the temporal and spatial dynamics of plasmas induced in liquids by nanosecond Nd:YAG laser pulses 1—Analysis of the plasma starting times," *Appl. Opt.*, vol. 27, pp. 3661–3668, 1988.
 - [42] J. Yellaiah and P. P. Kiran, "Characteristics of transient underwater acoustic signal from laser-induced plasma formation," *2019 Workshop on Recent Advances in Photonics (WRAP)*, 2019, pp. 1–3.
 - [43] V. Jukna, S. Albert, C. Millon, B. Mahieu, R. Guillermin, G. Rabau, D. Fattaccioli, A. Mysyrowicz, A. Couairon, and A. Houard, "Control of the acoustic waves generated by intense laser filamentation in water," *Optics Express*, vol. 30, no. 6, p. 9103, 2022.
 - [44] D. Horvat, V. Agrež, T. Požar, B. Starman, M. Halilović, and R. Petkovšek, "Laser-induced shock-wave-expanded nanobubbles in spherical geometry," *Ultrasonics Sonochemistry*, vol. 89, p. 106160, 2022.
 - [45] D. C. Rao, V. S. Mooss, Y. N. Mishra, and D. Hanstorp, "Controlling bubble generation by femtosecond laser-induced filamentation," *Scientific Reports*, vol. 12, no. 1, 2022.
 - [46] F. Blackmon, L. E. Estes, G. Fain and L. Antonelli, "Non-linear Optoacoustic Narrowband Communications Technique," U.S. patent 7613074B1, 2009.
 - [47] T. G. Jones, M. Helle, D. Kaganovich, A. Ting, M. Nicholas, D. Calvo, G. DiComo, and J. Caron, "Underwater Laser Acoustic Source Control using shaped plasmas," *The Journal of the Acoustical Society of America*, vol. 137, no. 4, pp. 2200–2200, 2015.
 - [48] F. Blackmon and L. Antonelli, "Remote, Aerial, Trans-Layer, Linear and Non-Linear Downlink Underwater Acoustic Communication," *OCEANS 2006*, pp. 1–7, 2006.
 - [49] T.G. Jones, M. Helle, A. Ting, and M. Nicholas, "Tailoring Underwater Laser Acoustic Pulses," *NRL REVIEW, acoustics*, pp. 142–143, 2012.
 - [50] T. G. Jones, A. Ting, J. Penano, P. Sprangle, and L. D. Bibee, "Remote Intense Laser Acoustic Source," *NRL Review*, 121–123, 2007.
 - [51] Y. Tagawa, S. Yamamoto, K. Hayasaka, and M. Kameda, "On pressure impulse of a laser-induced underwater shockwave," *J. Fluid Mech.*, Col. 808, No. 5, 2016.
 - [52] Y. Tian, L. Wang, B. Xue, Q. Chen, and Y. Li, "Laser focusing geometry effects on laser-induced plasma and laser-induced breakdown spectroscopy in bulk water," *Journal of Analytical Atomic Spectrometry*, vol. 34, no. 1, pp. 118–126, 2019.
 - [53] G. Sinibaldi, A. Occhicone, F. Alves Pereira, D. Caprini, L. Marino, F. Michelotti, and C. M. Casciola, "Laser induced cavitation: Plasma generation and breakdown shockwave," *Physics of Fluids*, vol. 31, no. 10, p. 103302, 2019.
 - [54] H. Jiang, H. Qiu, N. He, and X. Liao, "Research on the optoacoustic communication system for speech transmission by variable laser-pulse repetition rates," *Results in Physics*, vol. 9, pp. 1291–1296, 2018.
 - [55] Z. Ji, Y. Fu, J. Li, Z. Zhao and W. Mai, "Photoacoustic Communication from the Air to Underwater Based on Low-Cost Passive Relays," *IEEE Communications Magazine*, vol. 59, no. 1, pp. 140–143, January 2021.
 - [56] M. S. Islam, M. Younis, M. Mahmud, G. Carter, and F.-S. Choa, "A peak detection based OOK photoacoustic modulation scheme for air to underwater communication," *Optics Communications*, p. 129078, 2023.
 - [57] Z. Xu, L. Shen and J. Wang, "An Improved Differential Pulse Position Modulation Using Soft-Decision Decoding," *Proc. Int'l Conf on Wireless Comm., Networking and Mobile Comp.*, 2007, pp. 1373–1376.
 - [58] U. Sethakaset and T. A. Gulliver, "Differential amplitude pulse-position modulation for indoor wireless optical channels," *Proc. IEEE Global Telecommunications Conf. (GLOBECOM '04)*, pp. 1867–1871, 2004.

- [59] M. S. Islam, M. Younis, M. Mahmud and J. B. Saif, "A Novel Encoding Scheme for Improving the Bandwidth Efficiency of DPPM," *Proc. IEEE International Conference on Communications (ICC 2021)*, pp. 1-6, 2021.
- [60] "Focus Tunable Lenses." Optotune. Accessed June 26, 2023. [Online]. Available: <https://www.optotune.com/focus-tunable-lenses>.
- [61] "Round, Step-Variable, Metallic Neutral Density Filters." Thorlabs. Accessed June 26, 2023. [Online]. Available: https://www.thorlabs.com/newgrouppage9.cfm?objectgroup_id=1394.
- [62] O. Onasami, D. Adesina, and L. Qian, "Underwater Acoustic Communication Channel modeling using Deep Learning," *The 15th International Conference on Underwater Networks & Systems*, 2021.
- [63] L. Huang, Y. Wang, Q. Zhang, J. Han, W. Tan and Z. Tian, "Machine Learning for Underwater Acoustic Communications," in *IEEE Wireless Communications*, vol. 29, no. 3, pp. 102-108, June 2022.
- [64] D. Li-Da, W. Shi-Lian and Z. Wei, "Modulation Classification of Underwater Acoustic Communication Signals Based on Deep Learning," *2018 OCEANS - MTS/IEEE Kobe Techno-Oceans (OTO)*, pp. 1-4, 2018.
- [65] L. C. Domingos, P. E. Santos, P. S. Skelton, R. S. Brinkworth, and K. Sammut, "A survey of underwater acoustic data classification methods using Deep Learning for Shoreline Surveillance," *Sensors*, vol. 22, no. 6, p. 2181, 2022.
- [66] K. E. Frasier, "A machine learning pipeline for classification of cetacean echolocation clicks in large underwater acoustic datasets," *PLOS Computational Biology*, vol. 17, no. 12, 2021.
- [67] Y. Zhang, J. Chang, Y. Liu, X. Shen and W. Bai, "Deep Learning based Underwater Acoustic OFDM Receiver with Joint Channel Estimation and Signal Detection," *Proc. IEEE Int'l Conf. on Signal Processing, Communications and Computing (ICSPCC)*, pp. 1-5, Xi'an, China, 2022.
- [68] M. A. R. Ahad, A. D. Antar, and M. Ahmed, "Methodology of Activity Recognition: Features and Learning," in *IoT Sensor-Based Activity Recognition: Human Activity Recognition*, vol. 173. Cham, Switzerland: Springer, 2021, pp. 27-62.
- [69] R.-C. Chen, C. Dewi, S.-W. Huang, and R. E. Caraka, "Selecting critical features for data classification based on machine learning methods," *Journal of Big Data*, vol. 7, no. 1, 2020.
- [70] D. Iwai, H. Izawa, K. Kashima, T. Ueda, and K. Sato, "Speeded-up focus control of electrically tunable lens by sparse optimization," *Scientific Reports*, vol. 9, no. 1, 2019.
- [71] W. Morris, "The Well at the World's End," *The Project Gutenberg eBook of The Well at the World's End, by William Morris*. [Online]. Available: <https://www.gutenberg.org/cache/epub/169/pg169-images.html>. [26-June-2023].
- [72] M. R. Rafi, M. A. Salam, and O. Kandara, "Machine learning based attack detection in internet of things network," *Int'l Journal of Computer Science and Information Security (IJCSIS)*, vol. 19, no. 8, August 2021.
- [73] P. R. Ovi, E. Dey, N. Roy and A. Gangopadhyay, "ARIS: A Real Time Edge Computed Accident Risk Inference System," 2021 IEEE International Conference on Smart Computing (SMARTCOMP), pp. 47-54, Irvine, CA, USA, 2021.
- [74] W. H. Thorp, "Analytic description of the low-frequency attenuation coefficient," *J. Acoust. Soc. Am.*, vol. 42, no. 1, pp. 270-270, 1967.
- [75] H. W. Marsh and M. Schulkin, "Report on the status of Project AMOS Tch," U.S.Navy Underwater Sound Lab., New London, CT, 1952.
- [76] M. Stojanovic, "On the relationship between capacity and distance in an underwater acoustic communication channel," *ACM SIGMOBILE Mobile Comput. Commun. Rev.*, vol. 11, no. 4, pp. 34-43, Oct. 2007.
- [77] R. Coates, *Underwater Acoustic Systems*, New York: Wiley, 1989.

Choa has sponsored a total of more than \$19 million in research funding from different sources. He has authored and co-authored more than 410 refereed publications. He is a Fellow of OSA and SPIE. He served as editors of Optics Letters, Journal of High-Speed Networks, and Sensors.



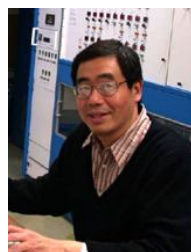
Muntasir Mahmud is currently a Ph.D. candidate and working as a research assistant in the department of computer science and electrical engineering at the University of Maryland Baltimore County (UMBC). He received M.S. in Electrical Engineering from UMBC and B.S. in Electrical and Electronic Engineering from the Islamic University of Technology (IUT). Before joining UMBC, he worked as a Radio Access Network (RAN) Engineer for Huawei and Nokia in Bangladesh.

He was a recipient of the Best Paper Award in WOCC 2021. His research interests are in the area of wireless communications, signal processing, and machine learning.



Mohamed Younis is currently a professor in the dept. of computer science and electrical engineering at the University of Maryland Baltimore County (UMBC). Before joining UMBC, he was with Honeywell International Inc., where he led multiple projects for building dependable computing infrastructure. He also participated in the development of the

Redundancy Management System, which is a key component of the Vehicle and Mission Computer for NASA's X-33 space launch vehicle. Dr. Younis' technical interest includes network architectures and protocols, cyber-physical systems, fault tolerant computing, secure communication and IoT networks. He has published over 350 technical papers in refereed conferences and journals. Dr. Younis has seven granted and four pending patents. In addition, he serves/served on the editorial board of multiple journals and the organizing and technical program committees of numerous conferences. Dr. Younis is a Fellow of the IEEE and the IEEE communications society.



Fow-Sen Choa received his B.S. degree from National Taiwan University, and his M.S. and Ph.D. degrees from SUNY at Buffalo. After his Ph.D. work on femtosecond infrared lasers and detectors, in 1988 he joined AT&T Bell Labs at Holmdel and Murray Hill, NJ and worked in the area of photonic integrated circuits and chemical beam epitaxy. Since joining UMBC in 1991, he has been working in the areas of semiconductor material, photonic devices, optical switches/networks, RF-photonic devices and cascade lasers, photon counting detectors, photoacoustic sensing and communications, nanostructures and metamaterials, brain imaging and brain stimulations. Since 1991, Prof.



Akram Ahmed received his MS degree in Electrical Engineering in 2008, from the University of Southern California, Los Angeles, USA, and his Ph.D. in Computer Engineering in 2019, from the University of Maryland Baltimore County, USA. He is currently an assistant professor in the Computer Engineering Department of King Fahd University of Petroleum and Minerals, Saudi Arabia. His research interest includes acoustic communication, communication protocols, and machine learning.